

JOINT INSTITUTE FOR NUCLEAR RESEARCH

**Annotation on Project
“MPD. MultiPurpose Detector”**

02-0-1065-2007/2023

LEADER

V.M.Golovatyuk, V.D.Kekelidze

Submitted

LHEP Science and Technology Council

THE LIST OF PARTICIPANTS FROM JINR AND MEMBER-STATES

Joint Institute for Nuclear Research, Dubna, RUSSIA (FTE=114)

K.Afanaciev, S.Afanaciev, G.Agakishiev, S.Andreeva, T.Andreeva, N.Anfimov, A.Aparin, V.Astakhov, G.Averichev, A.Averyanov, V.Babkin, I.Balashov, M.Barabanov, D.Baranov, A.Baskakov, P.Batuyk, A.Bazhazhin, S.Bazylev, A.Belyaev, E.Belyaeva, D.Blaschke, D.Bogoslovsky, I.Boguslavski, M.Buryakov, A.Butenko, A.Buturin, S.Buzin, V.Chalyshev, V.Cheplakova, V.Chepurnov, V.I.Chepurnov, G.Cheremukhina, P.Chumakov, B.Dabrowska, D.Dementiev, V.Didishko, A.Dmitriev, V.Dodokhov, A.Dolbilov, D.Dąbrowski, D.Donetz, A.Drapeza, A.Dubrovin, P.Dulov, N.Dunin, V.Dunin, V.Dziatlau, A.Efremov, D.Egorov, E.Streletskaya, V.Elsha, N.Emelianov, O.Fateev, Y.Fedotov, J.Fedotova, A.Fedunin, I.Filippov, M.Gaganova, O.Gavrishuk, S.Gerasimov, K.Gertsenberger, V.Golovatyuk, N.Gorbunov, A.Guskov, A.Isupov, A.Ivanov, V.Jejer, S.Kakurin, M.Kapishin, L.Kartashova, A.Kechechyan, G.Kekelidze, V.Kekelidze, G.Khodzhibagiyan, V.Kireyeu, Y.Kiriushin, I.Kiryutin, A.Kolesnikov, V.Kolesnikov, A.Kolozhvari, V.Komarov, A.Kovalenko, V.Kramarenko, L.Krasnova, Y.Krechetov, I.Kruglova, S.Kukarnikov, S.Kuklin, R.Lednickiy, A.Litomin, A.Litvinenko, E.Litvinenko, G.Litvinova, V.Lobanov, Y.Lobanov, S.Lobastov, A.Loseu, J.Lukstins, D.Madigozhin, V.Maksimenkova, A.Malakhov, I.Malikov, L.Malinina, D.Melnikov, S.Mertz, I.Meshkov, V.Mialkovski, I.Migulina, Y.Minaev, S.Mituxin, N.Molokanova, I.Moshkovskiy, A.Moskovsky, S.Movchan, A.Mudrokh, Y.Murin, G.Musulmanbekov, A.Nechaevskiy, V.Nikitin, I.Oleks, A.Olshevski, O.Orlov, S.Pargicky, V.Pavlyukevich, V.Penkin, V.Peresedov, E.Pervyshina, M.Peryt, D.Peshekhonov, A.Pilyar, S.Piyadin, A.Potanina, Y.Potrebenikov, D.Prahina, S.Razin, N.Ridinger, O.Rogachevsky, V.Rogov, K.Roslon, M.Rumyantsev, A.Rybakov, Z.Sadygov, V.Samsonov, C.Ceballos Sanchez, A.Savenkov, S.Savitskiy, T.Semchukova, A.Semenov, I.Semenova, S.Sergeev, N.Sergeeva, E.Serochkin, A.Shabunov, B.Shchinov, A.Shchipunov, A.Sheremetiev, A.Sheremetieva, M.Shitenkov, K.Shtejer Diaz, A.Shunko, A.Shutov, V.Shutov, A.Sidorin, A.Skulkin, I.Slepnev, V.Slepnev, I.Slepov, A.Sorin, T.Strizh, N.Sukhov, S.Sukhovarov, N.Surkov, V.Svalov, N.Tarasov, V.Tchekhovski, A.Terletskiy, O.Teryaev, V.Tikhomirov, A.Timoshenko, V.Toneev, N.Topilin, V.Trofimov, G.Trubnikov, I.Tyapkin, S.Udoenko, V.Vasendina, S.Vereshagin, N.Vladimirova, N.Vlasov, A.Vodopyanov, S.Volgin, O.Volodina, A.Voronin, G.Yarigin, V.Yurevich, M.Zaiceva, N.Zamyatin, S.Zaporozhets, A.Zinchenko, D.Zinchenko, V.Zruev, A.Zubarev

A.I.Alikhanyan National Science Laboratory, ARMENIA

H.Grigorian, A.Ayriyan, V.Abgaryan, A.Piloyan

National Nuclear Research Center, AZERBAIJAN

A.Rustamov, R.Satarov

University of Plovdiv, BULGARIA

B.Dabrowska, P.Dulov, N.Geraksiev, M.Ilieva, D.Suvarieva, V.Tcholakov, L.Yordanova

Universidad Tecnica Federico Santa Maria, Valparaiso, CHILE

S.Kovalenko, S.Kuleshov, L.L.N.Paredes, R.R.Caballero, E.F.R.Calderon, P.A.U.Poblete, N.V. Maria, J.A.Zamora Saa

Central China Normal University, CHINA

F.Liu, X.Sun, Y.Wang

Huzhou University, CHINA

F.Wang, J.Wang, X.Zhu

Institute of High Energy Physics, CHINA

M.Huang, M.Weiz, K.Xu

Institute of Modern Physics of the Chinese Academy of Sciences, Lanzhou, CHINA

Z.Li, X.Niu, Y.Wang, N.Xu, H.Yang, Yapeng Zhang, Yuezhao Zhang, C.Zhao, W.Zhou

Shandong University, CHINA

C.Feng, J.Jiao, Q.Xu, C.Yang, D.Liu

Fudan University, CHINA

Y.Ma, D.Fang, W.He

Three Gorges University, CHINA

S.Feng, K.Wu, X.Yuan, S.Li

Tsinghua University, Beijing, CHINA

Z.Deng, G.Gong, B.Guo, D.Han, Y.Huang, Y.Li, H.Miao, C.Shen, Y.Wang, Z.Xiao, Z.Xu, X.Zhu, P.Zhuang, Z.Zou

University of South China, CHINA

X.Wang

University of Science and Technology of China, Hefei, CHINA

Z.Tang, W.Zha, Z.Li, P.Lu

Nuclear Physics Institute of Czech Academy of Sciences, CZECH Republic

A.Kugler, V.Kushpil, S.Kushpil, V.Mikhaylov, O.Svoboda, P.Tlustý

Palacky University, Olomouc, CZECH Republic

J.Kvita, M.Maslan, L.Nožka, T.Rössler

Tbilisi State University, Tbilisi, GEORGIA

T.Babutsidze, G.Kachlishvili, A.Machavariani, M.Nioradze, R.Shanidze

Benemérita Universidad Autónoma de Puebla, MEXICO

E.Moreno Barbosa, M.Rodríguez Cahuantzi, G.Tejada Muñoz, V.Z.Reyna Ortíz, C.H.Zepeda Fernández

Centro de Investigación y de Estudios Avanzados, MEXICO

M.A.Ayala Torres, L.M.Montaña Zetina, M.A.Fontaine Sánchez

**Instituto de Ciencias Nucleares de la Universidad Nacional Autónoma de México,
MEXICO**

M.Alvarado, A.Ayala, W.Bietenholz , L.Díaz, M.E.Patiño

Universidad Autónoma de Sinaloa, MEXICO

I.Domínguez Jiménez, P.A.Nieto Marín

Universidad de Colima, MEXICO

M.E.Tejada-Yeomans

Universidad de Sonora, MEXICO

L.Valenzuela Cazares, A. Guirado Garcia, J. C.Maldonado Gonzalez,
I.A.Maldonado Cervantes, L.Rebolledo, E.Cuautle

Institute of Applied Physics, Chisinev, MOLDOVA

M.Baznat, D.Baznat, A.Khvorostukhin

Jan Kochanowski University, POLAND

P.Kankiewicz, M.Rybczynski, G.Stefanek, Z.Wlodarczyk

National Center for Nuclear Reseach, Otwock – Swierk, POLAND

A.Bancer, M.Bielewicz, A.Chłopik, A.Dudziński, M.Grabowski, K.Grodzicki, E.Jaworska,
S.Mianowski, M.Pietrzak, J.Rzadkiewicz, P.Sibczyński, Ł.Świdorski, A.Syntfeld

University of Warsaw, POLAND

W.Dominik, I.Skwira-Chalot, T.Matulewicz, M.Kuich, K.Piasecki, D.Wójcik

Warsaw University of Technology, Warsaw, POLAND

M.Czarnynoga, D.Dąbrowski, G.Kasprowicz, A.Kisiel, M.Ławryńczuk, M.Linczuk, M.Peryt,
S.Plamowski, J.Pluta, K.Poźniak, P.Rokita, R.Romaniuk, K.Rosłon, T.Starecki, T.Traczyk,
P.Wieczorek, D.Wielanek, W.Zabołotny

University of Wroclaw, POLAND

D.Blashke, N.-U.Bastian, U.Shukla

Belgorod National Research University, RUSSIA

A.Klyuev, A.Kubankin, R.Nazhmudinov, K.Vokhmyanina

Institute for Nuclear Research of the Russian Academy of Sciences, Moscow, RUSSIA

A.Botvina, M.Golubeva, F.Guber, A.Ivashkin, A.Izvestnyy, N.Karpushkin, A.Kurepin,
S.Morozov, O.Petukhov, A.Strizhak, V.Volkov

National Research Nuclear University MEPHI, Moscow, RUSSIA

E.Alpatov, E.Atkin, N.Barbashina, A.Demanov, O.Golosoov, E.Kashirin, P.Kulyamin,
G.Nigmatkulov, V.Nikolaev, P.Parfenov, A.Povarov, V.Samsonov, I.Selyuzhenkov,
V.Shumikhin, M.Strikhanov, A.Taranenko

Moscow Institute of Physics and Technology, RUSSIA

T.Aushev

North Ossetian State University, Vladikavkaz, RUSSIA

N.Pukhaeva, Y.Kasumov, A.Eremina, A.Korsunov, D.Kibizov, Z.Persaeva, R.Esenov

**National Research Center "Kurchatov Institute" – Institute of Theoretical and
Experimental Physics, Moscow, RUSSIA**

V.Kulikov, M.Martemianov, M.Matsyuk, S.Bulychjov

National Research Center "Kurchatov Institute", Moscow, RUSSIA

D.Blau, D.Peresunko

Petersburg Nuclear Physics Institute, Gatchina, RUSSIA

A.Ezhilov, O.Fedin, V.Guzey, D.Ivanishchev, A.Khazadeev, L.Kochenda, D.Kotov,
P.Kravchov, E.Kryshen, A.Kyrianova, M.Malayev, V.Maleev, Y.Naryshkin, D.Pudzha,
Y.Riabov, V.Samsonov, V.Solovyev, A.Vasilyev, M.Vznuzdaev, M.Zhalov, V.Riabov

Skobeltsyn Institute of Nuclear Physics, Lomonosov Moscow State University, RUSSIA

N.Baranova, G.Bogdanova, E.Boos, M.Cheremnova, G.Eyyubova, D.Karmanov, P.Kharlamov,
O.Kodolova, M.Korolev, V.Korotkikh, A.Kryukov, V.Kukulin, D.Lanskoy, I.Lokhtin,
L.Malinina, M.Merkin, M.Platonova, G.Romanenko, A.Solomin, T.Tretyakova, V.Volkov,
E.Zabrodin

Saint Petersburg State University, RUSSIA

I.Altsybeev, E.Andronov, S.Belokurova, E.Boykova, V.Chulikov, V.Chulikov, A.Erokhin,
G.Feofilov, S.Igolkin, V.Il'in, V.Kakichev, V.Kondratev, V.Kovalenko, T.Lazareva, N.Makarov,
N.Maltsev, A.Merzlaya, D.Nauruzbaev, D.Nesterov, D.Prokhorova, N.Prokofiev, A.Puchkov,
A.Rakhmatullina, V.Sandul, A.Seryakov, K.Sevastianova, O.Sobol, M.Tkachev, S.Torilov,
F.Valiev, V.Vechernin, A.Zarochentsev, V.Zherebchevsky

TABLE OF CONTENTS

1. Introduction.....	6
2. Physics motivation.....	8
3. MPD detector.....	11
3.1 Introduction.....	11
3.2 Superconducting Magnet.....	13
3.3 Time Projection Chamber – TPC.....	15
3.4 TOF identification system.....	20
3.5 The Status of the FFD.....	22
3.6 Forward Hadron Calorimeter (FHCAL).....	22
3.7 Electromagnetic Calorimeter (ECAL)	23
3.8 MPD Data Acquisition (DAQ) system and computer cluster.....	27
4. Recent results of MPD performance and feasibility study.....	29
4.1 MPD tracking and particle ID performance.	29
4.2 Bulk properties: hadron spectra, yield, and ratios	31
4.3 MPD performance for (multi)strange hyperon production.....	33
4.4 Direct and elliptic flow measurements at NICA/MPD.....	35
4.5 Study of electron-positron pairs in A+A collisions at NICA/MPD...36	
5. Milestones of MPD assembling in 2020-2021.....	37
6. Funding.....	38

1 Introduction

The project "Multipurpose detector MPD for studying the properties of hot and dense baryon matter at the collider complex NICA" is devoted to a detailed exploration of the QCD phase diagram and search for the signals of deconfinement phase transition and the critical endpoint [1]. Comprehensive investigations in the unexplored region of the phase diagram of strongly interacting matter will be performed by a careful energy and system-size scan with ion species ranging from protons to Au^{79+} over the energy range $4 < \sqrt{s_{NN}} < 11$ GeV. The goal of the Project is to design and build a multifunctional detector to measure heavy-ion collisions and investigate the basic Quantum Chromo Dynamics structure of matter. A vast research program in heavy-ion collisions (HIC) has been carried out over last 20 years and a number of new phenomena were discovered. There is a strong evidence for a deconfinement phase transition in central HIC at low SPS energies [2]. Extensive experimental data collected by the RHIC experiments [3] suggest formation of a new state of dense partonic matter - strongly interacting Quark-Gluon Plasma (sQGP). However, it is commonly believed that a next generation of heavy ion experiments is required for much more sensitive and detailed study of the QCD phase diagram in the region of large baryochemical potential μ_B [4]. Several accelerator centers have

recently started new programs with heavy ions: SPS at CERN [5], RHIC at BNL[6] and CBM at FAIR [7] may be considered as complementary programs aimed at the study of relevant physics problems of hot and dense baryonic matter.

The main advantages of the NICA/MPD project is that the NICA accelerator facility will provide a vast choice of beams (from protons to gold ions) in the energy range which brackets onset of deconfinement (center-of-mass energy from 4 to 11 GeV). A high luminosity of NICA ($L = 10^{27} \text{cm}^{-2}\text{s}^{-1}$) allows small enough energy steps and provide high interaction rate. The key feature of the proposed MPD detector design that allows studying of nuclear collisions with high precision are:

- High event rate (up to 6 KHz) allows very subtle measurements of the energy and centrality dependence of any phenomenon under interest
- MPD has full azimuthal coverage and will measure most of the momentum range in the pseudo-rapidity interval $-2 < \eta < 2$.
- Tracking and particle identification system including TPC for energy loss and TOF for time-of-flight measurements complemented by an electromagnetic calorimeter for photons and electrons with good time and energy resolution.

The existing international collaboration aimed in the Project realization consists of about 450 scientists from 16 Institutions from Russia and abroad.

References

- [1] A.N. Sissakian and A.S. Sorin, J. Phys. G: Nucl. Part. Phys. 36 (2009) 064069.
- [2] C.Alt et al.Phys.Rev.C 77, 2008, 024903.
- [3] Nucl.Phys. A757 (2005), 1-283
- [4] Searching for a QCD mixed phase at the NICA (NICA White paper). Draft v2.01, 30 September 2009. <http://nica.jinr.ru/>
- [5] NA61 experiment. CPOD07 (2007),023. Eprint=0709.1646.
- [6] G.S.F. Stephans, J. Phys., G32 (2006), S447-S454.
- [7] P.Senger, J. Phys. G30 (2004), S1087-S1090.
- [8] The MultiPurpose Detector (MPD). Conceptual Design Report, v1.0.
<http://nica.jinr.ru/>

2 Physics motivation

A vast research program in heavy-ion collisions (HIC) has been carried out over recent years and a number of new phenomena were discovered. The diversity of the experimental landscape of HIC data, obtained at the AGS, SPS, RHIC and LHC, is already quite rich and impressive. One may start here with referring to the studies of NA49 collaboration at SPS in investigations of the phase diagram of strongly interacting matter and there is a strong evidence for a deconfinement phase transition in central HIC at low SPS energies [1]. Extensive experimental data collected by the RHIC experiments [2] suggest formation of a new state of dense partonic matter - strongly interacting Quark-Gluon Plasma (sQGP). Recently, the main scientific goals of the Beam Energy Scan (BES) program included the search for the onset of the deconfinement and scan of the phase diagram with variable collision energy from 200 GeV down to a few GeV. The BES program at RHIC produced a wealth of results to describe the bulk properties of the medium created in Au+Au reactions for collision energies of 7.7, 11.5, 19.6, 27, 39, 62.4 and 200 GeV by measuring hadron production at midrapidity. However, it is commonly believed that a next generation of heavy ion experiments is required for much more sensitive and detailed study of the QCD phase diagram in the region of large baryochemical potential μ_B . In Fig. 2.1 (left panel), the dynamical trajectories at two collisions energies are shown for central ($b = 2$ fm) Au + Au collisions. The highly non-equilibrium part of trajectories are calculated within the kinetic Quark Gluon String Model (shown by open symbols) and the subsequent evolution (filled symbols) is evaluated within the 3D relativistic hydrodynamics [3].

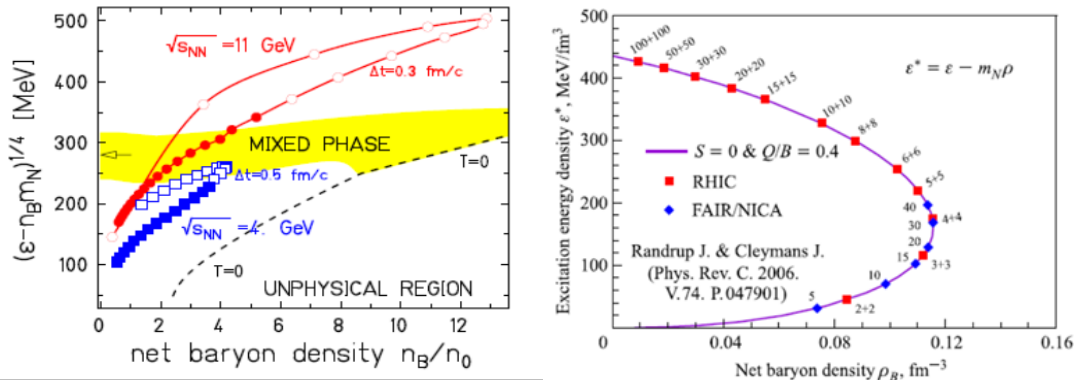


Fig. 2.1: (Left) The phase diagram in terms of the reduced energy density and net baryon density. The highlighted region is a quark-hadron mixed phase estimates according to the phenomenological two-phase equation of state [3]. The dashed curve separates the unphysical region by condition $T = 0$. (Right) Correlation of the net baryon density and the excitation energy density in central Au+Au collisions [4].

The fascinating particularity of this region is that the nuclear matter at highest net baryon density is achieved (see Fig. 2.1, right panel) [4], as well as new states of matter beyond the deconfinement and chiral transitions.

At present, several complementary experimental programs throughout the world are planned to further study heavy-ion reactions at lower energies. In particular, nucleus-nucleus collisions at the NICA accelerator complex at JINR (Dubna, Russia) permit the exploration of the nuclear matter properties in the region where the baryon density increases substantially. The new experimental program planned at high intensity NICA beams will bring deeper insight into the dynamics of hadronic interactions and multiparticle production mechanisms in the expected high baryonic density regime [5]. Furthermore, the investigation of the properties of nuclear matter inside neutron stars is the key goal of modern astrophysics. The recent observation of the neutron star merger both via gravitational waves [6] began the new era of multi-messenger astronomy. Recent model calculations reveal that in the neutron star merger process nuclear matter reaches densities and temperatures expected in the heavy-ion collision in the NICA energy range. Therefore, the MPD experimental NICA offers unique opportunity to study such processes in the laboratory.

The global scientific goal of the NICA/MPD project is to explore the QCD phase diagram in the region of highly compressed and hot baryonic matter. In particular, the fundamental QCD phenomena, such as confinement, properties of the QCD vacuum and QCD Lagrangian symmetries, quantitative understanding of which is still lacking, will be addressed. In particular, the NICA/MPD project will be focused on the study of the in-medium properties of hadrons and the nuclear matter Equation Of State (EOS), including a search for possible signals of deconfinement and/or chiral symmetry restoration phase transitions, as well as the QCD critical endpoint (CEP) in the region of the collider energies $\sqrt{s_{NN}} = 4 - 11$ GeV. The basic experimental strategy will to measure a large variety of signals systematically changing collision parameters (energy, centrality and system size). Reference data (i.e. pp and pA collisions) will be taken in the same experimental conditions. A tentative list of experimental observables includes:

- a) the yields, spectra, and ratios for multiple probes from gammas to light nuclei;
- b) event-by-event fluctuations and correlations;
- c) collective flow of identified hadron species;
- d) strangeness production in dense baryon matter, including multistrange hyperons and hypernuclei;
- e) femtoscopy; d) electromagnetic probes (electrons and gammas). The hadrons containing heavy strange quarks and anti-baryons are of particular interest.

According to lattice QCD calculations a phase transition from the hadronic phase to the phase composed of deconfined quarks and gluons is suggested at energy density exceeding a value of about $0.5 \sim \text{GeV}/\text{fm}^3$. Microscopic model calculations indicate such a density can be achieved in the center of the fireball created in head-on collisions of gold ions at center-of-mass energies above 4-5 GeV. The deconfinement transition is found to be a crossover at zero net-baryon density [7], while arguments based on effective models predict that it becomes a first-order transition at some finite chemical potential [8]. It implies the existence of a critical end point (CEP) in the phase diagram of the QCD matter separating both phase transition types [9]. The potentially rich structure of the QCD phase diagram at high net-baryon densities requires experimental verification. The QCD phase diagram structure might be tested by measuring abundances of different hadron

species, while different regions of the diagram are accessible by varying the collision energy. Existing experimental results on hadron abundances in the range from AGS to LHC energies indicate that the final state of HIC is close to chemical equilibrium, thus the yields are fitted by the statistical thermal model with two free parameters: temperature T and baryochemical potential μ_B . Assuming that the measured multiplicities are preserved throughout final hadron-resonance cascade expansion, their analysis reveals the hadronization point along the QCD parton-hadron boundary line. Moreover, the analysis of hadron abundances might (potentially) allow to address the much debated onset of deconfinement problem. If HIC dynamics within the NICA energy range crosses the phase transformation line starting from a particular (threshold) energy, then, below this value, the actual hadronic multiplicity would not stem from the QCD hadronization phase transition (responsible for chemical equilibration among the species) and we would expect a sizeable change in the observed hadronic freeze-out pattern, such as a sequential chemical freeze-out in inverse order of inelastic cross-section.

REFERENCES

- [1] C. Alt et al. (NA49 Collab.), *Phys. Rev. C* 77, 024903 (2008).
- [2] RHIC Experiment White Papers, *Nucl. Phys. A* 757, 1-283 (2005).
- [3] A.S. Khvorostukin et al., *Eur. Phys. J. C* 48 (2006), 531-543.
- [4] J. Randrup and J. Cleymans *Phys. Rev. C* 74 (2006) 047901.
- [5] V. D. Kekelidze, R. Lednicky, V. A. Matveev, I. N. Meshkov, A. S. Sorin and G. V. Trubnikov, *Eur. Phys. J. A* 52, 211 (2016).
- [6] Abbott, B. P. et al. (LIGO Collab.), *Phys. Rev. Lett.* 119, (2017), 161101.
- [7] Aoki Y., Endrodi G., Fodor Z., Katz, S. D., Szabo K. K., *Nature* 443 (2006) 675-678.
- [8] Asakawa M., Yazaki K., *Nucl. Phys. A* 504 (1989), 668-684.

3. MPD detector

3.1 Introduction

The MPD apparatus has been designed as a 4π spectrometer capable of identifying charged hadrons, electrons and photons in heavy-ion collisions in the energy range of the NICA collider and measuring their momenta. To reach this goal, the detector will comprise a precise 3-D tracking system and a high-performance particle identification (PID) system based on the time-of-flight measurements and calorimetry. The basic design parameters has been determined by physics processes in nuclear collisions at NICA and by several technical constrains guided by a trade-of of efficient tracking and PID against a reasonable material budget. At the design luminosity, the event rate in the MPD interaction region is about 6 kHz; the total charged particle multiplicity exceeds 1000 in the most central Au+Au collisions at $\sqrt{s_{NN}} = 11$ GeV. As the average transverse momentum of the particles produced in a collision at NICA energies is below 500 MeV/c, the detector design requires a very low material budget. The general layout of the MPD apparatus is shown in Fig.3.1.1. The whole detector setup covering ± 2 units in pseudorapidity (η).

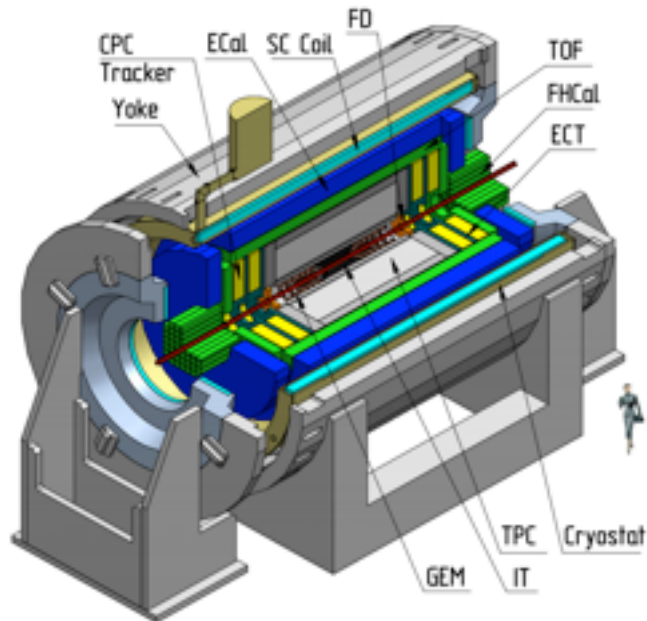


Fig. 3.1.1: Full Configuration of the MPD consists of Magnet Yoke (Yoke) and Solenoid (SC Coil), Time Projection Chamber (TPC), Time of Flight System (TOF), Fast Forward Detector (FFD), Forward hadron Calorimeter (FHCAL), Forward Tracker (CPC and ECT) and Inner tracker System (IT)

As soon as construction of such detector requires long period of time, large group of physicists, engineers and technicians and large funds there was decision to build it in two stages.

The aim of this Project is to build the first stage of the MPD setup (Fig.3.1.2), which consists of the Magnet based on superconducting solenoid, Time-Projection Chamber (TPC), barrel Time-Of-Flight, Forward Calorimeter (FHCAL) and Fast Forward Detector (FD).

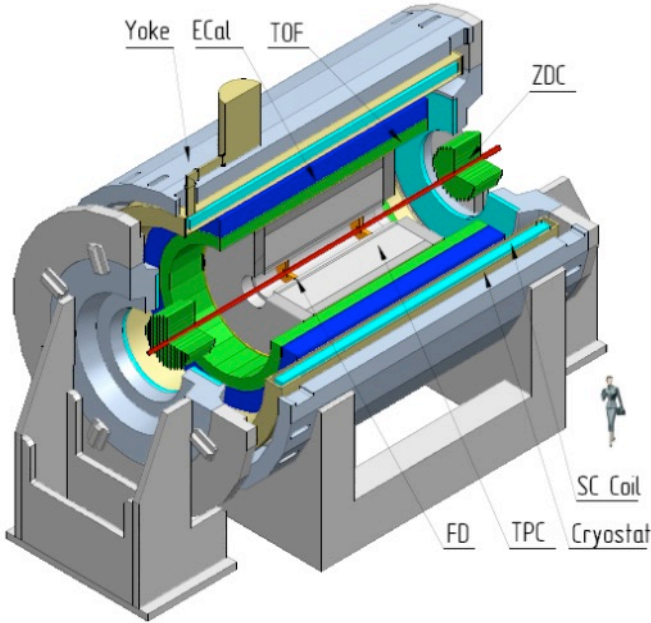


Fig. 3.1.2: The MPD setup in the first Stage. It consists of Magnet Yoke, Solenoid, Time Projection Chamber (TPC), Time of Flight detector (TOF), Electromagnetic Calorimeter (ECal), Fast Forward Detector (FFD) and Forward Hadron Calorimeter (FHCAL)

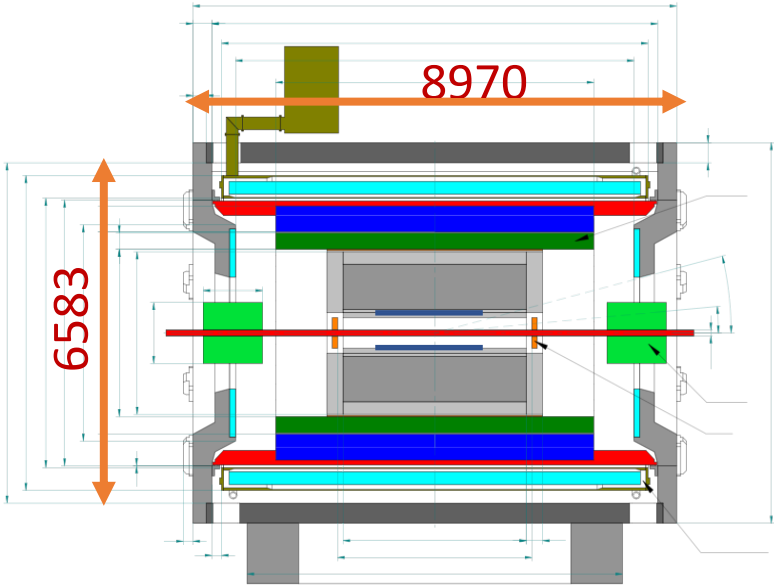


Fig. 3.1.3: Cutaway side view of the MPD in a basic Configuration with main dimensions.

The MPD is a 9 m long cylinder of about 6,6 m in diameter. The cross-sectional view of the MPD Detector in base configuration is shown in Fig. 3.1.3.

3.2 Superconducting magnet

The magnet of the MPD detector is intended to provide a homogeneous magnetic field with a rated value of magnetic field of 0.5 T inside its aperture. The required volume average inhomogeneity in the drift volume of TPC (of about 2.4 m in diameter and 3,4 m long) -

$$\text{Integral}(B_r/B_z) \cdot dz \leq 1,5\text{mm}.$$

The superconducting magnet of MPD is intended for providing a highly homogeneous magnetic field of 0.57 T ensure the transverse momentum resolution within the range of 0.1–3 GeV/c at NICA. A constituent part of the MPD is a solenoid with a superconducting NbTi coil and a steel flux return yoke.

The MPD magnet consists of (Fig. 3.2.1):

- a cryostat with a superconducting coil and a control Dewar;
- a flux return yoke with two support rings, 28 bars, and two poles with trim coils;
- magnet support cradles;
- auxiliary platforms for moving the poles;
- roller skates for movement of the magnet and its poles.

In addition, there are power supplies for the superconducting solenoid and for the trim coils in the poles, a SC coil quenching protection system, a cryogenic system with the cryogenic pipeline, a vacuum system, helium refrigerator and a magnet control system.

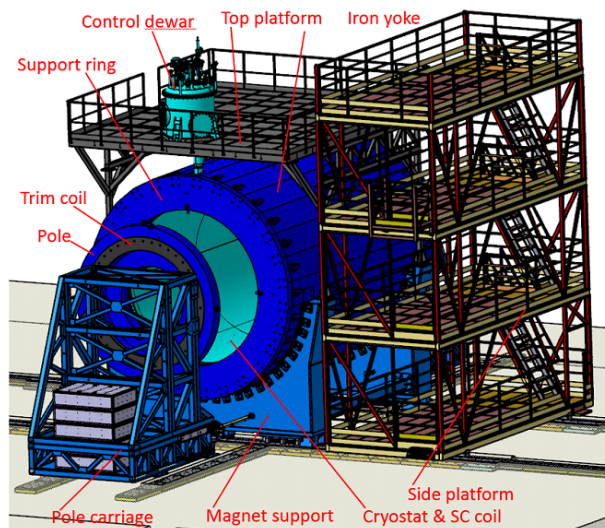


Fig. 3.2.1. Overall view of the magnet.

3.2.1 Solenoid

Rated current of the magnet is 1790 A (it corresponds to a field in the aperture of 0.5 T). The maximum magnet field at which the specified value of the integral of the radial component of the induction in the area of TPC $\text{Int} \leq 1.5 \text{ mm}$ is maintained, and which can be achieved with a maximum level of technological deviations from the optimized geometry of the magnetic system, is 0.57 T.

In 2015 the manufacturer company has been defined for production of the Solenoid and its auxiliary equipment such as power supplies, control and protection system, vacuum system etc. Then, in the end of 2015 related contract has been signed with ASG Superconductors s.p.a (Italy).

The complete assembly of the solenoid has been finished by September 2019 (Fig. 3.2.2). Since that moment the solenoid is ready for transportation to JINR's premises.



Fig.3.2.2 . Completely built solenoid.

3.2.2 Magnet Yoke

In 2012, the geometry of the MPD detector was adopted in the final version (Fig. 3.2.3). The length of the magnetic circuit was 8970 mm, the outer diameter - 6.63 m. The total weight of the magnetic circuit, consisting of 2 support rings, 2 poles and 28 beams, is 630 tons. The weight of the MPD detector in the design configuration is 980 tons.

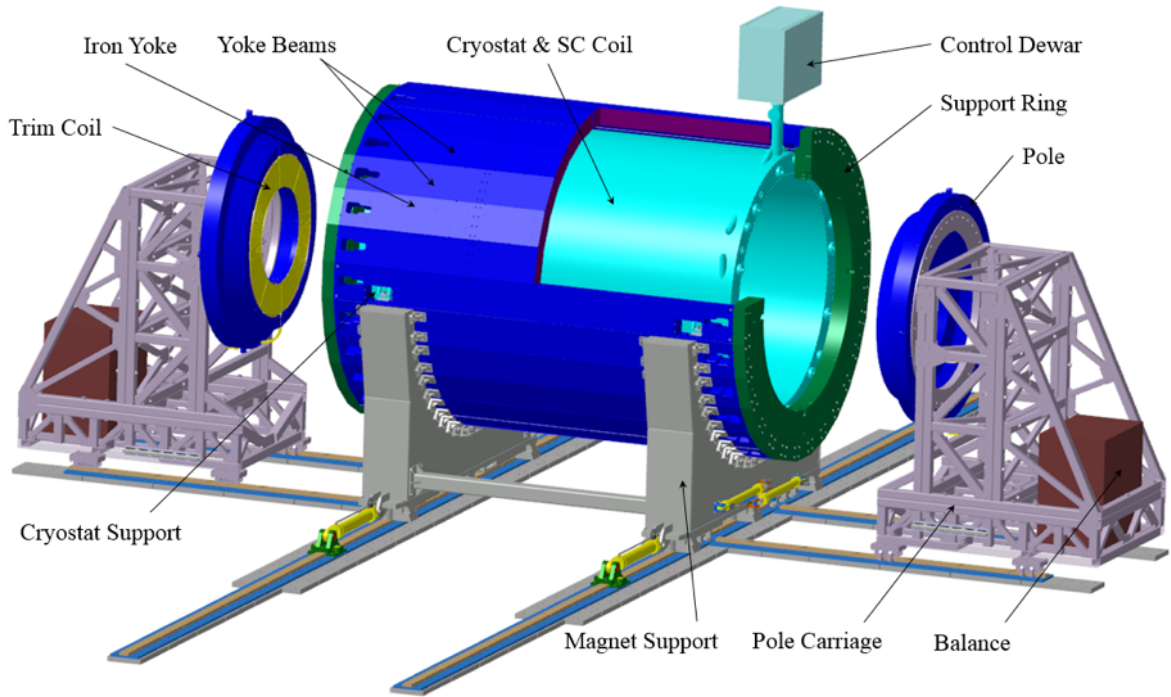


Fig. 3.2.3. MPD magnetic circuit with poles on transport supports.

3.3 Time Projection Chamber - TPC

The Time-Projection Chamber (TPC) is the main tracking detector of the MPD central barrel. It is a well-known detector for 3-dimensional tracking and particle identification for high multiplicity events. The TPC/MPD will provide:

- the overall acceptance of $\eta < 1.2$;
- the momentum resolution for charge particles under 3% in the transverse momentum range $0.1 < p_t < 1 \text{ GeV}/c$;
- resolution of two tracks of about 1 cm;
- hadron and lepton identification by dE/dx measurements with a resolution better than 8%.

These requirements must be satisfied at the NICA design luminosity with event rate about 6 kHz. Max charged particle multiplicity - up to 1000 tracks in central Au-Au collisions.

3.3.1. TPC design

TPC consists of four cylinders (C1-C4) manufactured by the Russian industry from composite materials. This approach provides sufficient cylinders strength along (in the worst case, the deformation at load of $F = 80 \text{ kG}$ in the middle is less than $100 \mu\text{m}$) and a small radiation thickness ($0.4 \text{ g}/\text{cm}^2$). All four cylinders are interconnected by two aluminum flanges. The gap between C1-C2 and C3-C4 is blow through by nitrogen N_2 for protection against a high-voltage discharges and prevention of H_2O and O_2 diffusion into the drift volume of the TPC.

The central high-voltage electrode-membrane divides the drift volume into two parts and creates the electric field strength which is necessary for the drift of the generated electron-ion clusters to

the TPC end-caps (see Fig. 3.3.1, pos. 2). The membrane is produced with the 110 μm Mylar film. The non-uniformity of magnetic field have to be not worse than $B_r/B_z \sim 10^{-4}$. The Field cage (see Fig. 3.3.1, pos. 3) has a symmetrical design, each part of which is located on both sides of the high-voltage electrode and consists from 112 pairs (outer and inner structures) of 13 mm wide mylar strips stretched on special rods with the same pitch and accuracy of 50 μm . The high-voltage electrode is connected to the nearest mylar strip by a resistor and each subsequent strip is connected by a resistor to the next one. This chain forms a HV divider from -24 kV (high voltage electrode) to zero (TPC end-caps).

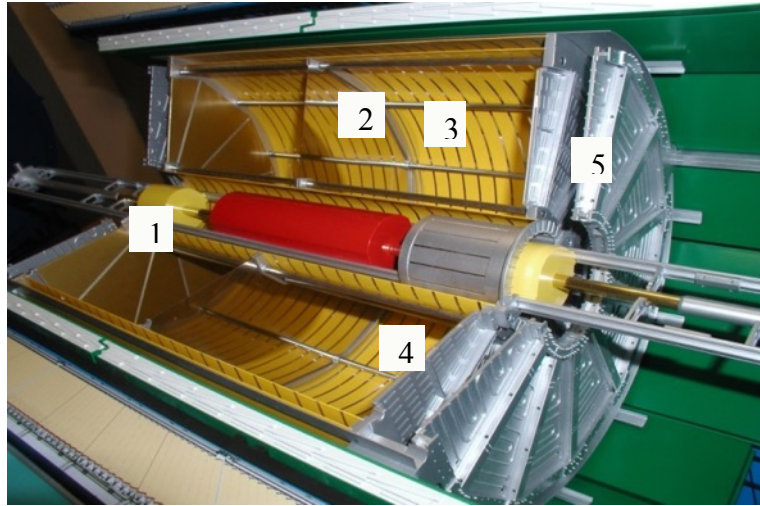


Fig. 3.3.1. Central part of the MPD (mock up). 1- MWPC; 2 - HV electrode; 3 - field cage; 4 – flange with MWPCs and FEE electronics; 5 - end cap thermal screen.

The main subsystems of TPC include:

- Readout Chambers (ROC)
- Gas System
- Laser Calibration System
- Cooling System
- FEE, Readout and DAQ
- DCS
- HV and LV systems

The basic design parameters of the TPC are summarized in Table 3.3.1.

Table 3.3.1

The basic parameters of the TPC

Item	Dimension
Length of the TPC	340 cm
Outer radius of vessel	140 cm
Inner radius of vessel	27 cm

Outer radius of the drift volume	133 cm
Inner radius of the drift volume	34 cm
Length of the drift volume	163 cm (of each half)
HV electrode	Membrane at the center of the TPC
Electric field strength	140 V/cm
Magnetic field strength	0.5 Tesla
Drift gas	90% Ar+10% Methane
Gas amplification factor	10^4
Drift velocity	5.45 cm/ μ s
Drift time	< 30 μ s
Temperature stability	< 0.5°C
Number of readout chambers	24 (12 per each end-plate)
Segmentation in ϕ	30°
Pad size	5x12 mm ² and 5x18 mm ²
Number of pads	95232
Pad raw numbers	53
Zero suppression	up to 90%
Maximal event rate	< 7 kHz (Lum. 10^{27})
Electronics shaping time	180-190 ns
Signal-to-noise ratio	30:1
Signal dynamical range	10 bit
Sampling rate	10 MHz
Sampling depth	310 time buckets
Resolution of two tracks	1 cm

3.3.2 Readout Chamber (ROC)

For the startup period of operation a ROC based on Multi-Wire Proportional Chambers (MWPC) with cathode pad readout and gate grid was chosen (see Fig. 3.3.1, pos.1). The gap between the anode wire plane and the cathode pad plane is the same as the gap between the anode wire and the cathode wire planes and is 3.0 mm. The anode wire pitch is set equal to $S=3$ mm and it is multiple to the pad length. Cathode wire pitch is 1.5 mm. The gate grid is placed 3 mm above the cathode wires and its wire pitch is 1.25 mm. Gate grid is used to stop the flow of ions from MWPC to TPC drift volume. To ensure the gas gain at the level of $G = 10^4$ with moderate anode wire potential, the 20- μ m diameter gold-plated tungsten–rhenium anode wire with tension 50 gram is used. The

75- μm diameter copper–beryllium wire wound under an 80-g force is used for the cathode plane. The pad geometry is selected based on the pad response function calculation and measurements to provide the required spatial resolution, and the number of pad rows is determined by the momentum resolution requirement. There are 27 rows of 5 \times 12 mm pads in the inner area of the pad plane and 26 rows of pads with dimensions 5 \times 18 mm in the outer area. The total number of registration channels of the TPC is 95232. Pad plane is produced by multilayer printed circuit board technology. It has 4 layers: a layer with pads, a layer with a ground plane, a layer with signal routing and a layer with connectors that are 1 mm apart from each other for a parasitic capacity minimization, which together give a total board thickness of 3 mm.

3.3.6 Front-End Electronics (FEE) and data readout system

The TPC FEE is based on ASIC[3], FPGAs and high-speed serial links (see Fig. 3.3.6). To protect the FPGA firmware from SEU, standard proprietary methods are suggested.

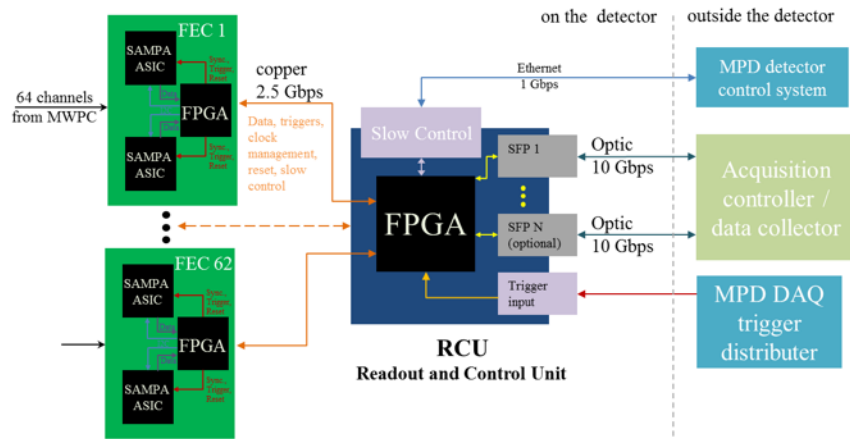


Fig. 3.3.6. Block diagram of data readout for one from 24 ROC chamber.

Each of 62 Front-End Cards (FECs), which are the basic elements of the data acquisition system from each ROC are controlled by common Readout and Control Unit (RCU). Each FEC has a separate bidirectional communication interface with the controller (cooper link, up to 2.5 Gbps), which is used for card management, data receiving, FEC condition monitoring and providing of synchronization, triggering and reset signals (Fig. 3.3.6). Each of the 62 FECs operate in parallel and independently of each other, which provide overall system throughput at this level. The base functions of the RCU are the following: FECs management, data receiving from FECs, FECs synchronization, slow control, transfer of data to data collector via the optical interface, communication with the general MPD detector control system via an Ethernet port.

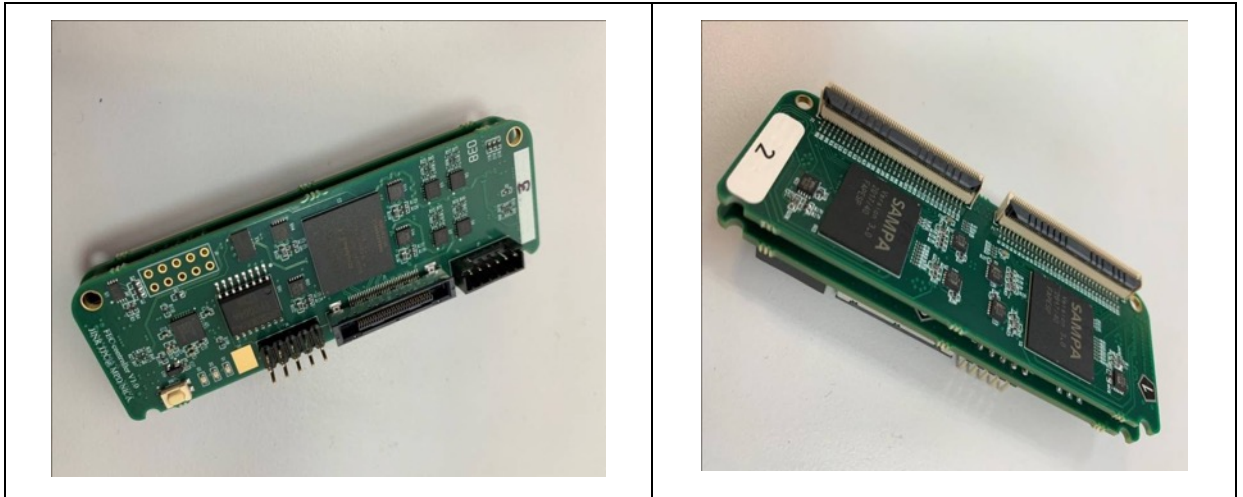


Fig. 3.3.7. FEC for TPC: top view (service side), left and bottom view (to padplane connected side), right.

Each of the 1488 FECs includes two ASICs called SAMP4 which was developed by USP Brazil electronics group mainly for upgrade ALICE experiment at CERN. The SAMP4 usage on cards made it possible to significantly reduce FEC size and due to it the radiation length of cards is about 3% X_0 (+ about 3% new cooling system). Another significant advantage of the new FEC is their ability to work with both positive and negative polarity of input signals. This feature will be useful in the future with a planned upgrade of ROCs from MWPC to GEM detectors.

Necessity not only to reduce the amount of material at the TPC end-caps, but also to distribute it evenly, has been forced to develop a new card from two boards (Fig. 3.3.7). The first board (Fig. 3.3.7, right) contains two SAMP4 chips giving in total of 64 independent registration channels. The SAMP4 amplifies the analog signal from the TPC pads, digitizes it with a 10-bit sampling ADC with a frequency of 10 MHz, processes it when the signal processor is enabled and transmits via serial links.

The second board (see Fig. 3.3.7, left) is a FEC controller. It is based on CYCLONE V GX FPGA. The FPGA performs the following main functions: high-speed bidirectional serial interface with the controller (up to 2.5 Gbps), SAMP4s management and configuration, data receiving from SAMP4s, FEC slow control features.

The first tests of the FECs showed their suitability for usage as TPC electronics. FPGA utilization in the data acquisition system provides us with great opportunities to further improvement of the system. The implementation of the FEC in the form of a double-desk board also gives us additional flexibility in the future upgrade of the system. If necessary, the controller part of the FEC can be replaced with another card, for example, with a flash-based FPGA (if it will be necessary due to radiation hard conditions of electronics operation).

3.3.7 TPC assembly and infrastructure

Since the TPC field cage containment cylinders are not differ significantly each form other in size the TPC assembling will be done at horizontal position of each elements. The arrangement for TPC assembling is shown schematically in Fig. 3.3.8. The pair of precisely positioned rails placed

on at surface, the strong "arm" I-beam with adjustable module, a system of three mobile and a special mobile platform create mechanical structure for step-by-step assembling of the TPC field cage elements.

The special assembly tooling was manufactured at Mechanical and Instrument Engineering Corporation (Bryansk, Russia) and was delivered to LHEP (see Fig. 3.3.9).

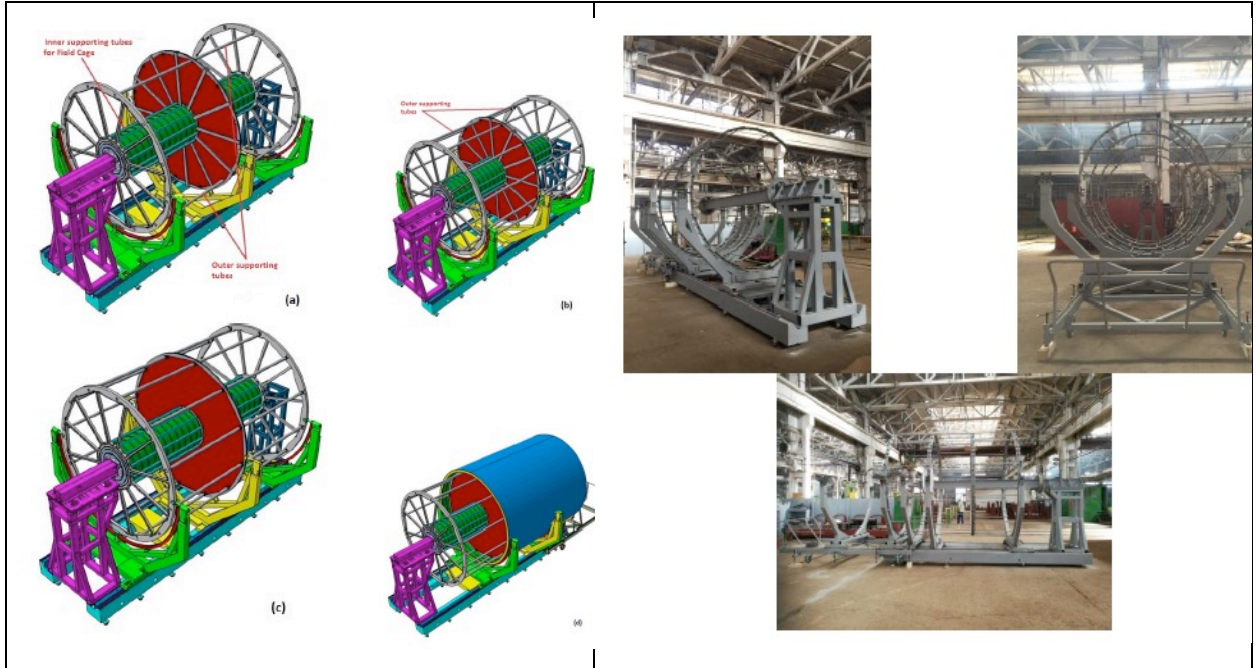


Fig. 3.3.8. TPC assembly steps

Fig. 3.3.9. Manufactured TPC assembly tooling

3.4 TOF identification system

The Time-of-Flight detector is basic charged hadrons identification system of multipurpose detector. In base configuration, the TOF will be represented as a barrel – cylinder length of about 6 meters and diameter of 3 meters assembled of 28 modules (Fig. 3.4.1). Each module contains 10 MRPC detectors (Fig. 3.4.2). The TOF detector system is organized in a modular way in order to minimize the number of components and cost. In addition to the TOF modules, the system includes the following service subsystems: low and high voltage power supplies, gas system, data acquisition electronics, cooling and slow control. Start configuration of the TOF system should be commissioned in 2020.

3.4.1 Multigap resistive plate chambers

Each TOF module consists of 10 identical multigap resistive plate chambers with 24 readout channels each. Development and testing of MRPC prototypes were performed in period of 2013 – 2017. We tested several different versions of MRPCs with cosmic rays and deuteron beam of Nuclotron. The final version of MRPC made of commercial float glass with a thickness of 280 μm . It has 15 gas gaps and provides time resolution around 50 ps.

During 2017-2018, all materials for the production of such MRPCs were purchased. Before mass production began, we had more than 90% of all necessary materials. Mass production of detector and modules started at the beginning of 2019. At the end of 2019, the production of 120 detectors and 10 modules will be completed. All modules production should be completed in 2020.

From the beginning of 2020, all TOF modules will be tested on cosmic rays stand, which was designed and commissioned especially for this goal in 2019.

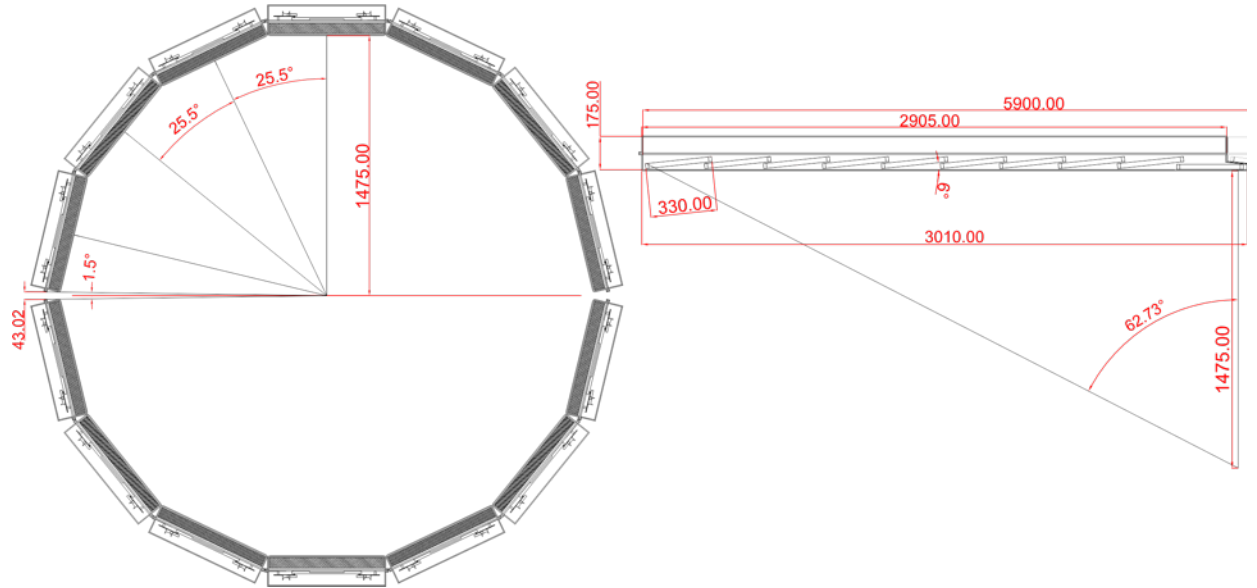


Fig. 3.4.1. Scheme of the TOF system barrel with overall dimensions.

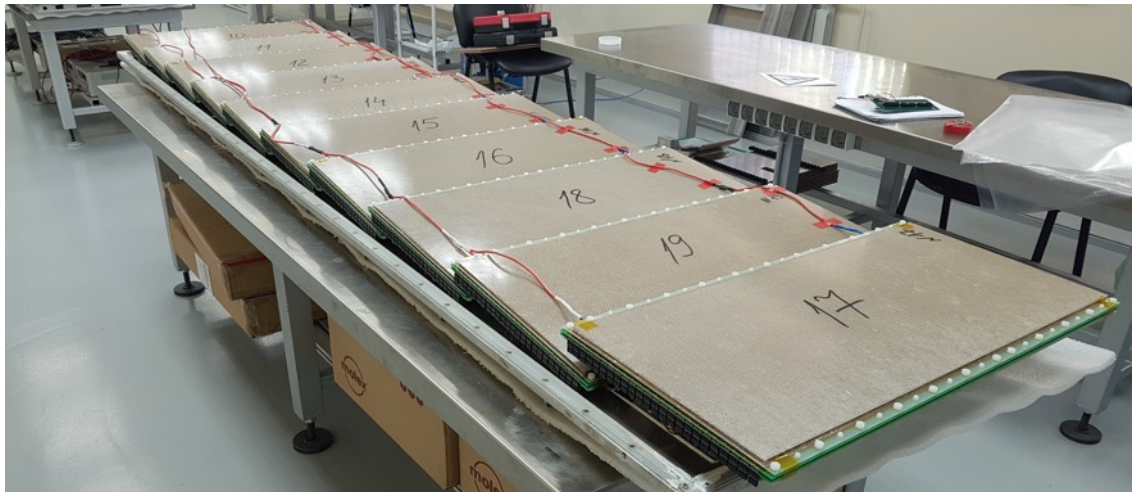


Fig. 3.4.2. Arrangement of MRPC detectors in the TOF module.

3.5. The Status of the FFD

The Fast Forward Detector (FFD) is important part of the MPD facility at the NICA collider [1] and its aim is to provide fast trigger of nucleus – nucleus collisions in center of the MPD setup and T0 pulse for TOF detector. The concept and technical details of the FFD are described in FFD TDR.

The block scheme of the FFD system, shown in Fig. 3.5.1, consists of two identical sub-detectors FFD_E and FFD_W based on 20 Cherenkov modules each, two units of sub-detector electronics (SDU) processing detector pulses, a trigger vertex electronics unit (VU), readout electronics, a picosecond laser calibration system, HV power supply, a detector control system (DCS), a cable system, a cooling system.

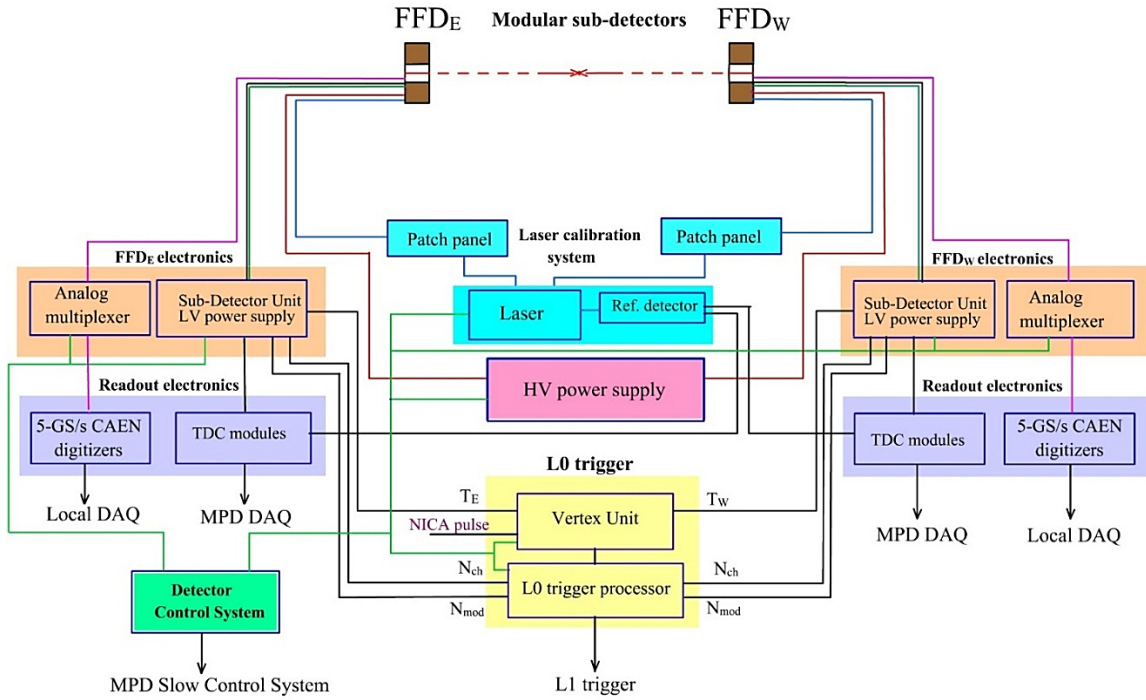


Fig. 3.5.1. A block-diagram scheme of the FFD system.

Each FFD sub-detector consists of 20 identical Cherenkov modules with 100- channel granularity. Each module consists of a 10- mm lead plate converter, four quartz bars of radiator, a photodetector MCP-PMT XP85012/A1, front-end electronics board, HV divider, module housing with connectors and cables.

3.6 Forward Hadron Calorimeter (FHCAL)

JINR and INR RAS (Moscow). This detector is one of the basic elements of MPD setup and is intended for the measurements of the geometry of heavy ion collisions. The main purpose of the FHCAL is to provide an experimental measurement of a heavy-ion collision centrality (impact parameter) and orientation of its reaction plane. Precise event by-event estimate of these basic observables is crucial for many physics phenomena studies to be performed with the MPD experiment.

FHCal consists of two identical arms placed upstream and downstream the beam collision point. The modular structure of one FHCal arm is presented in Fig. 3.6.1. Since the heavy fragments escape into beam holes, it is not possible to discriminate the central and peripheral collisions using only the deposited energies in FHCal. The subdivision of the calorimeter into two, inner and outer parts (see Fig. 1), and the calculation of the energy depositions E_{in} and E_{out} separately in these calorimeter parts allows the construction of new observable, energy asymmetry: $A_E = (E_{in} - E_{out}) / (E_{in} + E_{out})$. Taking the two-dimensional correlation between the energy asymmetry, A_E and full energy deposition in calorimeter, it is possible to resolve the ambiguity in central and peripheral events, respectively.

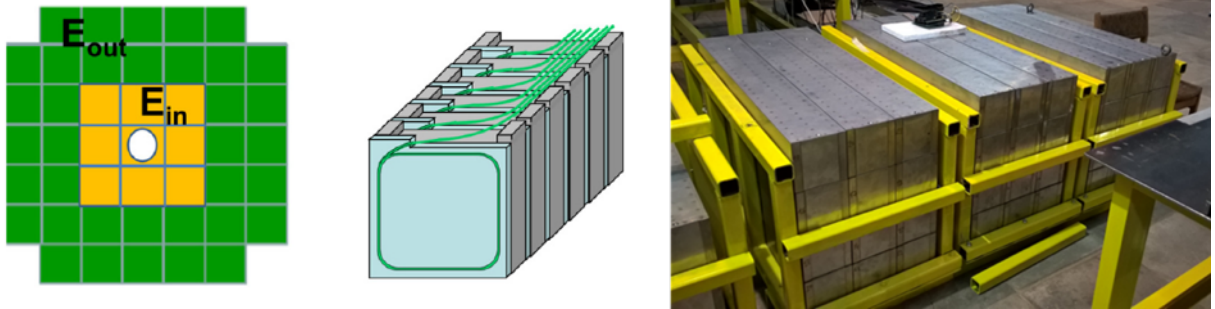


Fig. 3.6.1. Left— Front view of FHCal structure. It is subdivided into two (inner/outer) parts for the measurements of centrality. Center — structure of the individual module. Right – stack of produced modules ready for delivery to JINR.

3.6.1 FHCal module design

The FHCal module transverse sizes of 15×15 cm² were chosen to match the size of the hadron showers. Each FHCal module includes 42 lead-scintillator sandwiches with a sampling ratio 4:1 (the thickness of lead plates and scintillator tiles is 16 mm and 4 mm, respectively).

Each module of hadron calorimeter consists of 42 lead–scintillator tile sandwiches with the sampling ratio 4 : 1 (thickness of the lead plates and scintillator tiles are 16 and 4 mm, respectively) that satisfies the compensation condition. According to simulation, the sampling fluctuations provide the energy resolution of calorimeter as: $\sigma_E/E \sim \sqrt{55\%/E}$ (GeV) The beam tests of the calorimeter with the same sampling confirm the results of simulation.

3.7 ECal detector

The main goals of the calorimeter are the participation in particles identification (namely - final cleaning of the selected e^+e^- sample) and measurements of the photons flux as well as

reconstruction of some decays with participation of the photons. The final result depends on performances of other MPD detectors like TPC and TOF.

3.7.1 Design of the ECal

Large-sized (6-meters-long and 4.5-meters in diameter) electromagnetic barrel calorimeter (ECal) is an important part of the Multy-Purpose Detector (MPD) at heavy-ion NICA collider that covers the central pseudorapidity region of $|\eta| < 1.2$. ECal is optimized to provide precise spatial and energy measurements for photons and electrons in the energy range from about 40 MeV to 2-3 GeV. To deal with a high multiplicity of secondary particles from Au-Au reaction, ECal has a fine segmentation and consists of 38 400 cells -"towers", (Fig. 3.7.1). Taking all requirements (high energy resolution, large enough distance to the vertex, small Moliere radius, ability to work in the high magnetic field, high time resolution, resistance to radiation, and reasonable price) into consideration, a "shashlyk"-type electromagnetic calorimeter was selected. Each "tower" has a sandwich structure of 210 polystyrene scintillator and 210 lead plates with 16 Wave Length Shifting (WLS) fibers that penetrate the plates to collect the scintillation light; the thickness of each scintillator plate is 1.5 mm, and the thickness of lead plate is 0.3 mm (Fig. 3.7.2).

Design of the ECal was done on the basis of many MC studies that were performed during last years. As the result of MC studies, a decision was taken to build the calorimeter with the projective

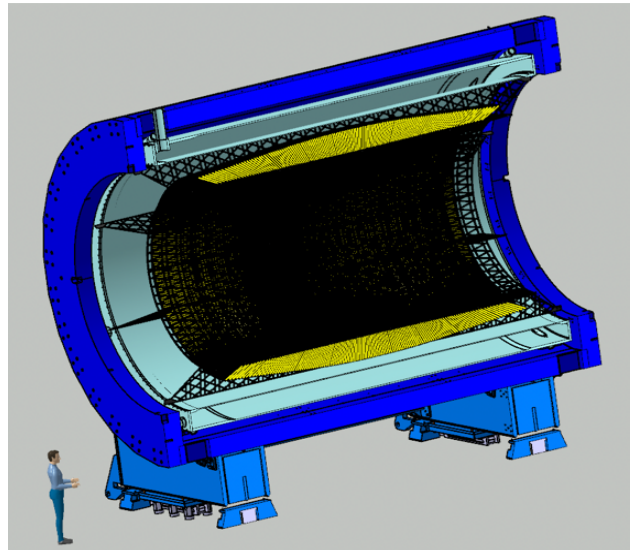


Fig. 3.7.1. View of the ECal inside of the Solenoid

geometry (Fig. 2.2.1.46) which is more complicated to construct than the simple structure that was planned in the beginning of ECal project (in the 2014). The main advantage of the new design is reduction of dead zones, increase of detector efficiency, improvement of linearity and energy resolution of the calorimeter measurements in conditions of high multiplicity of secondary particles from collisions of heavy ions. In the same time, the new design of the calorimeter is more complicated and demands more engineering efforts. Calorimeter modules production become more complex and time-consuming, and requires more manpower. The above-mentioned problems resulted in some delay in the preparation of the mass production of the calorimeter modules.

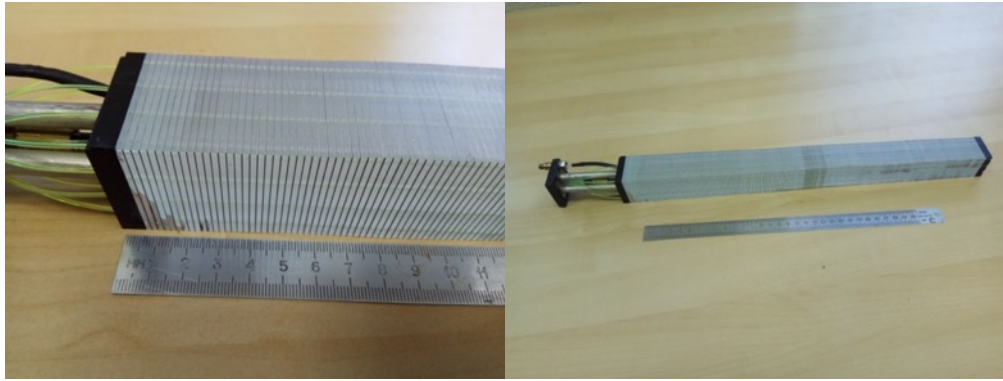


Fig. 3.7.2. Foto of the tower for ECal

Design of the ECal was done on the basis of many MC studies that were performed during last years. As the result of MC studies, a decision was taken to build the calorimeter with the projective geometry (Fig. 3.7.3) which is more complicated to construct than the simple structure that was planned in the beginning of ECal project (in 2014). The main advantage of the new design is reduction of dead zones, increase of detector efficiency, improvement of linearity and energy resolution of the calorimeter measurements in conditions of high multiplicity of secondary particles from collisions of heavy ions. In the same time, the new design of the calorimeter is more complicated and demands more engineering efforts.

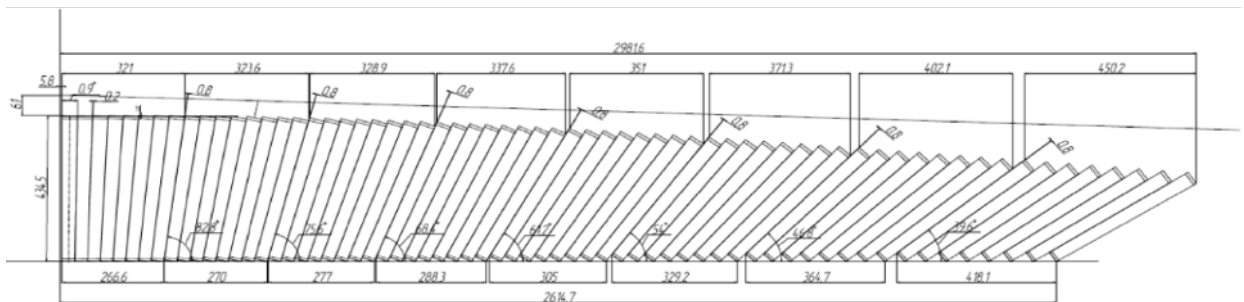


Fig. 3.7.3. Arrangement of the towers in the half-sector of the electromagnetic calorimeter with the projective geometry.

Each electromagnetic calorimeter module consists of 16 towers that are glued together. The geometry of each module depends on the module Z-coordinate location in respect to the beam interception point. To detect scintillation light that is collected by the 16 Wave Length Shifting (WLS) fibers that are passing through the holes in the scintillator and lead tiles, Hamamatsu S13360-6025 MAPD units were selected (with $6 \times 6 \text{ mm}^2$ sensitive area). Few modules of the new design (Fig. 3.7.4) have been produced and carefully tested using test beams and cosmic rays. Results of the tests are in the reasonable agreement with MC predictions.

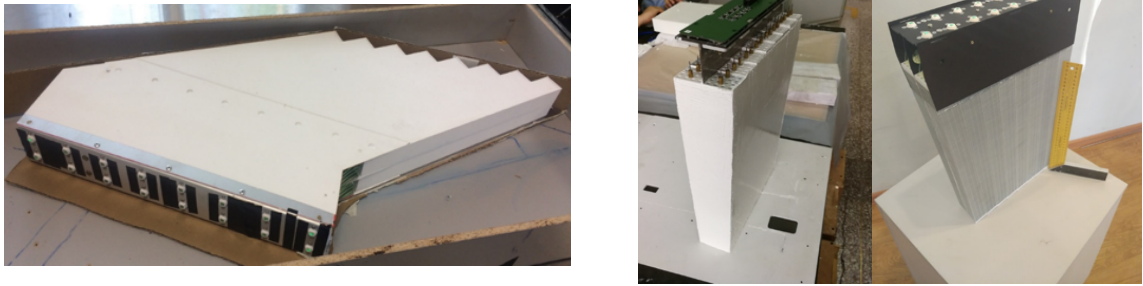


Fig. 3.7.4. Prototype modules. On the bottom-left panel, the readout electronics board is shown.

Geometrically, ECal is organized into 25 sectors or 50 half-sectors. Each half-sector (Fig. 3.7.6) contains 48 modules (of 8 different types) that are glued into a fiberglass container (basket) as well as correspondent readout and slow-control electronics with total mass of about 1.5 ton. Model calculations demonstrate that the cell structure of the basket with 2-mm-thick walls provides enough strength and rigidity to keep all possible deformations of the half-sector under its own weight under 0.5 mm for all possible orientations of half-sector in space. At the moment, a contract of production of 52 baskets is in the stage of final signing; we expect that 16 baskets will be delivered to JINR by October 2020, and whole number of baskets is expected to be delivered by Summer 2021.

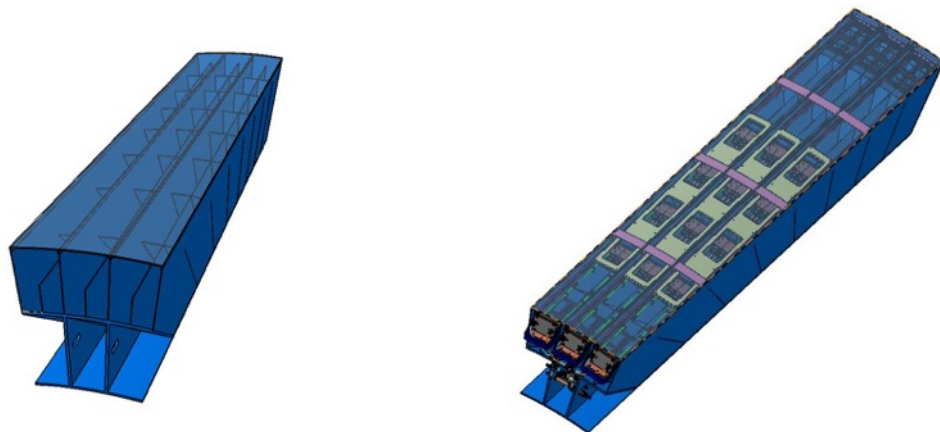


Fig. 3.7.6. ECal basket (left panel). Right panel shows the basket with installed readout electronics.

3.7.3 ECal integration

Originally, the electromagnetic calorimeter was planned as a self-supporting structure, where each sector contributes as a power element to the whole structure. But after splitting of the ECal modules production between Russian and Chinese sites (with different time schedules), ability to install and re-install calorimeter sectors (half-sectors) without whole calorimeter and MPD dismantle was requested. To meet this demand, we plan to use special support frame (about 8-meters-long and about 4.5-meters in diameter) made of carbon-fiber composite material that can hold whole load from MPD detectors without support from ECal sectors (Fig. 3.7.8). This frame will consist of inner (20-mm-thick) and outer (15-mm-thick) cylindrical shells with 25 bulkheads (10-mm-thick) in between them to form 25 cells for calorimeter sectors installation. Rigidity calculations for the

simplified frame model were performed and demonstrates that the planned total load of 120 tons will cause maximum frame deformations of about 2-3 mm that meets our demand to have deformations below 5 mm to keep ability of installation and re-installation of ECal half-sectors. Strength calculations assures the frame ability to hold the load about 10 times higher than our maximal expectations, and durability calculations and tests assures 15-year frame operation. At the moment, a contract of the frame design and production is in the stage of final signing; we expect the frame delivery to JINR by the November 2020.

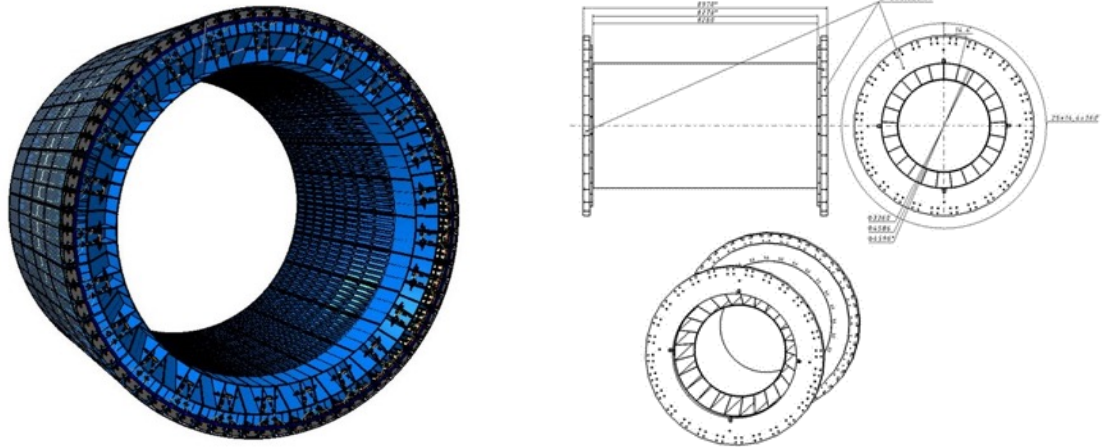


Fig. 37.8. The power frame of MPD. On the left panel, installed half-sectors are shown. The drawing on the right panel shows the frame fastening on the magnet support rings.

3.10.2 MPD DAQ network

On the present time a network equipment has bought for the MPD DAQ network (see network structure in Fig. 3.10.4). It is covering the test run needs, partially.

In 2020 will be planned to purchase:

- computing equipment FLP (480 cores) 10 servers;
- interim data storage TDS (must be required 500 TB of useable data volume) 10 servers;
- network equipment for a data acception from electronics and for a infrastructure needs in quantity 12 switches;
- servers for the MPD DAQ Network processes monitoring and logging in quantity 10 pieces.

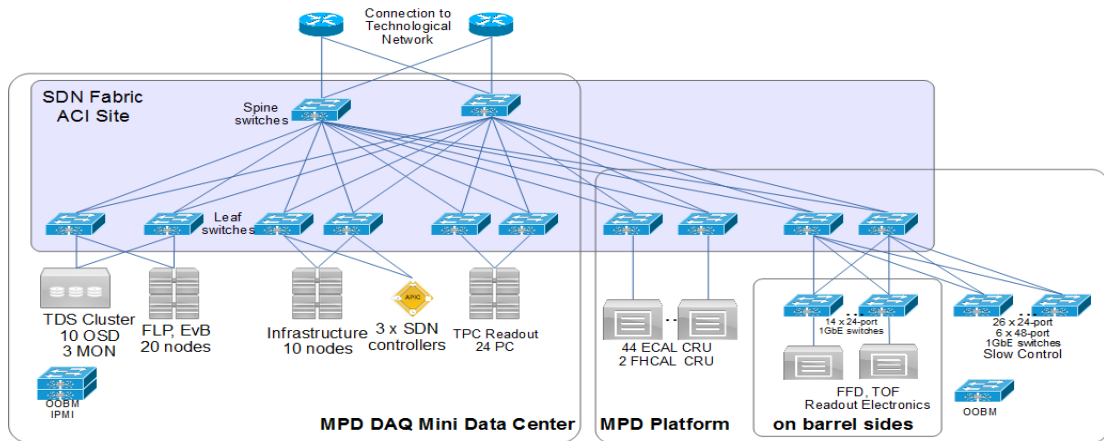


Fig. 3.10.4. MPD DAQ network structure.

Networking devices and DAQ electronics will be placed on and into the Barrel, at MPD platform and inside the MDC (see Fig. 3.10.5). At TPC, ECal and FHCAL readout electronics will be placed into the Barrel. The data from these detectors will be transmitted to the network devices for TPC and to the CRU-16 modules for ECal and FHCAL by optical links. Network devices and CRU-16 modules will be placed at the MPD platform. All aggregated by CRU-16 modules data will be transmitted to the MDC. Network devices and DRE at TOF and FFD detectors will be placed on the Barrel, around it. The data path is: from the DRE to the Network switches at platform, and from the Network switches to the MCD.

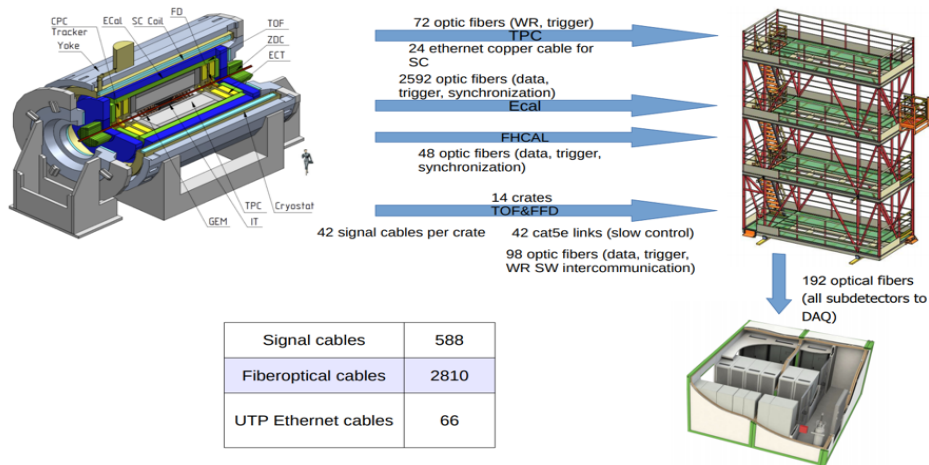


Fig. 3.10.5. MPD DAQ Network and DAQ Electronics

White Rabbit provides sub-nanosecond accuracy and picoseconds precision of synchronization for large distributed systems. It also allows for deterministic and reliable data delivery. DRE boards digitize detector signals using common notion of time and frequency provided by the White Rabbit (WR) network. The time reference is provided by GPS/GLONASS receiver and backup precision frequency reference (Cesium or Rubidium clock). the run control system.

4. Recent results of MPD performance and feasibility study

During 2016-20 a comprehensive program of MPD detector performance and feasibility studies was carried out. The results of these studies have been presented at many international conferences and published in refereed journals. Below, we summarize several selected results of this activity.

4.1 MPD tracking and particle ID performance.

Monte-Carlo simulations aimed in the optimization of the MPD design and performance study have been performed within a dedicated software framework - MpdRoot [1]. It includes an interface to a number of heavy ion event generators (UrQMD, DCM-LAQGSM, PHSD and others) and to the GEANT3 or GEANT4 transport packages. To obtain a realistic detector responses very detailed description of all the elements for each of the subdetectors was provided.

The track and vertex reconstruction methods are based on the Kalman filtering technique [2]. The implementation details can be found in Ref. [3]. The efficiency of track reconstruction is plotted as functions of transverse momentum and pseudorapidity in Fig. 4.1.1 for charged particles with at least 15 measured points in the TPC. One can see that the reconstruction quality remains quite high within the pseudorapidity range of $|\eta| < 1.5$ (with the efficiency near 100% and decent resolution) for both the primary and secondary particles with the secondary track sample on the plots containing particles produced within 50 cm of the interaction point.

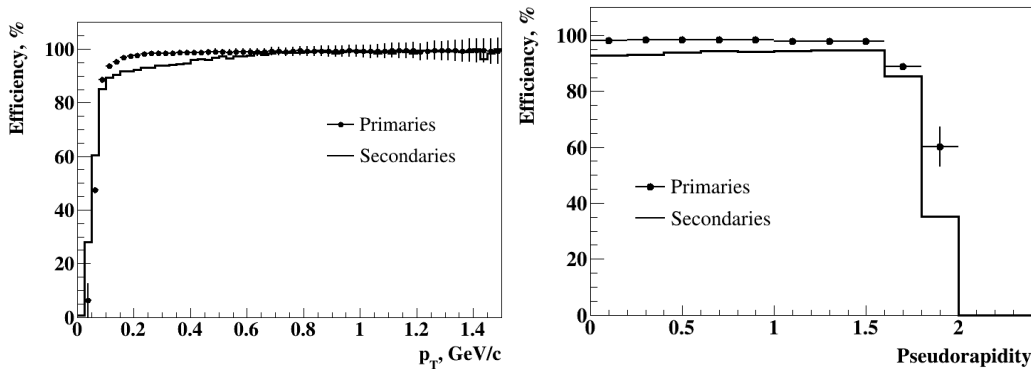


Fig. 4.1.1. Track reconstruction efficiency for particles with the number of measured points in the TPC (hits) greater than 14: (left) as a function of p_t for $|\eta| < 1.3$; (right) as a function of $|\eta|$ $p_t > 0.1$ GeV/c. Symbols and lines present primary and secondary particles, respectively. Secondary particles were produced within 50 cm from the interaction point.

An important characteristic of a detector is its ability to reconstruct vertices. It depends on the achievable accuracy of track pointing to the production point. Figure 4.1.2 (left panel) demonstrates the precision of the reconstructed interaction point (along the beam direction) as a function of the charged track multiplicity in the event. As can be seen, the accuracy of the primary vertex reconstruction varies from about 150 to 700 μm in central and peripheral collisions, respectively.

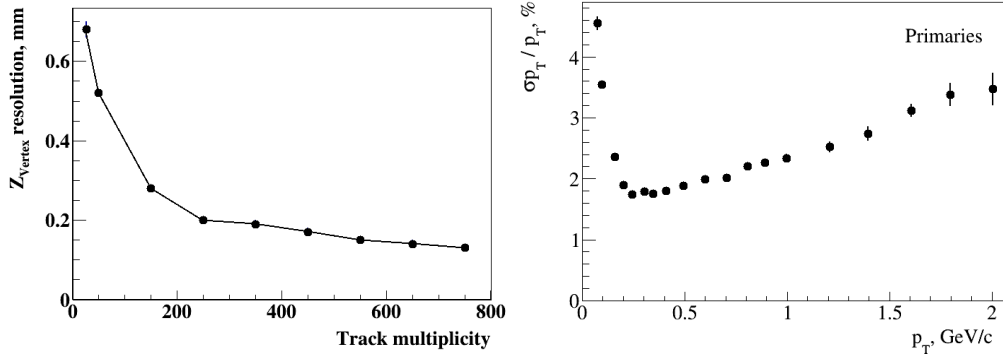


Fig. 4.1.2. Longitudinal position error of the reconstructed primary vertex as a function of track multiplicity.

The calculated relative momentum uncertainty $\Delta p_T/p_T$ is shown in Fig. 4.1.2 (right panel) as a function of p_T . It is seen from the plot that the resolution of less than 3% can be achieved at $p_T < 1.5$ GeV/c.

Particle identification (PID) in the MPD experiment will be achieved by using the information about the energy losses (dE/dx) in the TPC gas and the time-of-flight from the TOF detector. For optimal performance the PID procedure should rely on a good knowledge of the detector characteristics such as the momentum dependence of the average energy loss as well as the variation of the $\langle dE/dx \rangle$ and mass-squared resolutions for each particle specie. Based on this information a vector of probabilities to be a particle of a particular sort is assigned to each track and the highest probability defines the particle specie. As was demonstrated in Ref. [4], the achieved accuracy of the energy determination using the truncation value of 30%, i.e. rejecting 30% of the hits with the largest energy deposit before obtaining the mean value, is 6-7% (see Fig. 4.1.3), allowing discrimination of charged pions from kaons up to momenta of 0.7 GeV/c and kaons from protons up to 1.1 GeV/c.

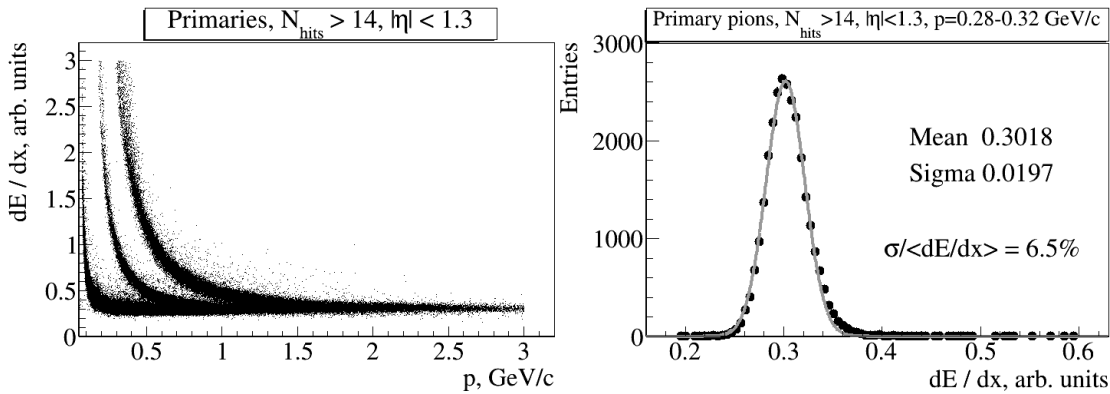


Fig. 4.1.3. (Left panel) Specific energy loss $\langle dE/dx \rangle$ as a function of momentum. (Right panel) Energy loss distribution for pions with $p = 0.28-0.32$ GeV/c fitted to the Gaussian.

The MPD TOF system (made of Multigap Resistive Plate Chambers - MRPCs) provides both the time and coordinate measurements with the accuracy of 80 ps and 0.5 cm, respectively. The MPD TOF performance for discrimination of hadrons in minimum bias Au+Au collisions at 9 GeV is demonstrated in Fig. 4.1.4, where on the left panel mass-squared as a function of the total momentum for positively charged hadrons from Au+Au collisions is shown, while on the right panel the fraction of the correctly identified particles is plotted as a function of momentum (dark

symbols). This fraction is above 90% for protons and positively charged pions up to $p=2.5$ GeV/c, while the percentage of the cases with a wrong identification is below 10%. As can be seen, we are able to identify charged kaons up to momentum of 1.7 GeV/c with an approximately 80% efficiency and 20% contamination at the PID limit. Making the selection criteria for kaons tighter, the achieved contamination level can be decreased further resulting in a lower value for the PID efficiency.

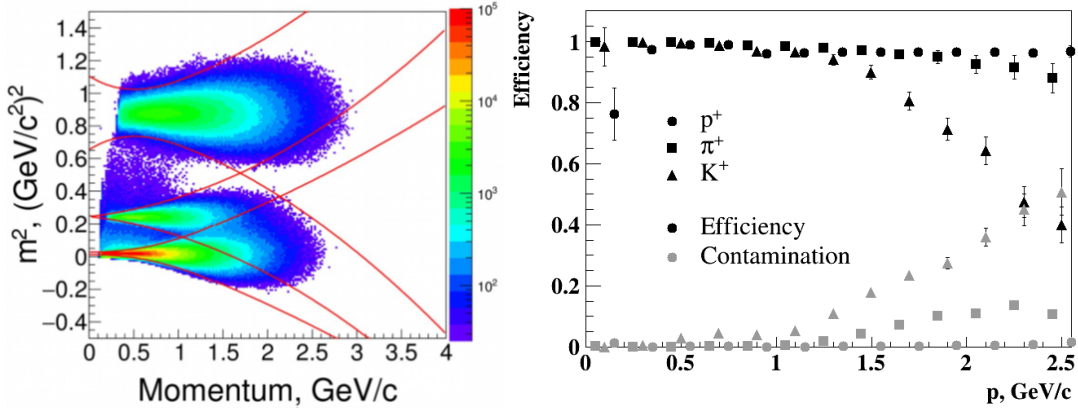


Fig. 4.1.4. (Left panel) Mass-squared as a function of the total momentum for positively charged hadrons from Au+Au collisions. (Right panel) Particle identification efficiency for positively charged hadrons (dark symbols) and a fraction of wrongly identified species (grey symbols) in Au+Au collisions at 9 GeV.

4.2. Bulk properties: hadron spectra, yield, and ratios

At NICA, a systematic study of particle yields and ratios will be performed as a function of collision energy, centrality, and kinematic variables (rapidity, transverse momentum, and azimuthal angle). The results of such a multi-parametric scan within the NICA energy range will be compared with the measurements in A+A (p+p) collisions at RHIC and SPS and to model calculations. For the discussed hadron measurements, the MPD detector will provide large and uniform acceptance for identified hadron species (see Fig. 4.2.1), allowing reconstruction of the total yields of mesons.

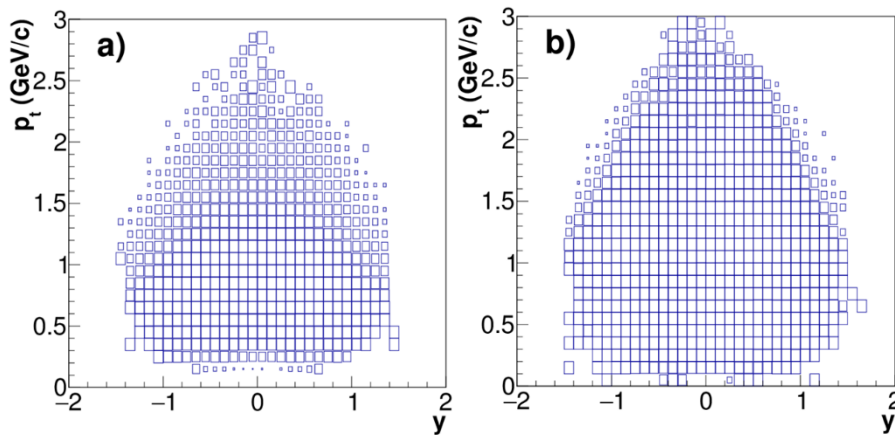


Fig. 4.2.1. The MPD phase space coverage in terms of rapidity and transverse momentum in Au+Au collisions at 8.8 GeV for identified K^+ (a) and π^+ (b). Note that the CM beam rapidity at this energy $y_{\text{beam}}=2.2$.

For the First-Day Physics period one among the probes will be the study of the production of charged pions and kaons near the maximum in the strangeness-to-entropy ratio (kaon-to-pion ratio has a non-monotonic behavior described as the "Horn" near the onset of the deconfinement phase transition at collision energy of about 8-9 GeV). In order to estimate the sensitivity of the proposed MPD detector setup to the potential phase transformation signals in dense nuclear matter via the ratio of strange hadrons to pions, a detailed Monte-Carlo study has been performed with the PHSD event generator, implementing both deconfinement and chiral symmetry restoration effects. We used data sets of 0-5% central Au+Au events at 5 collision energies (4, 6.2, 7.6, 8.8, 12.3 GeV) of 50 kEvents each. As an example, the invariant transverse momentum spectra of identified K^+ in rapidity bins are shown in Fig. 4.2.2 (left panel). As can be seen, with the suggested MPD setup we are able to measure hadron spectra up to $p_T=2.5$ GeV/c. In order to obtain the yield of hadrons in rapidity bins dN/dy , the reconstructed p_T spectra need to be extrapolated into unmeasured transverse momentum regions exploiting information on the spectral shape. For this, spectra were tested against a hydrodynamically inspired blast-wave (BW) model (dashed lines indicate the fit results). The results on dN/dy as a function of rapidity for positively charged pions and kaons are plotted in Fig. 4.2.2 (right panel). The quoted uncertainties are the quadratic sums of the statistical and systematic uncertainties.

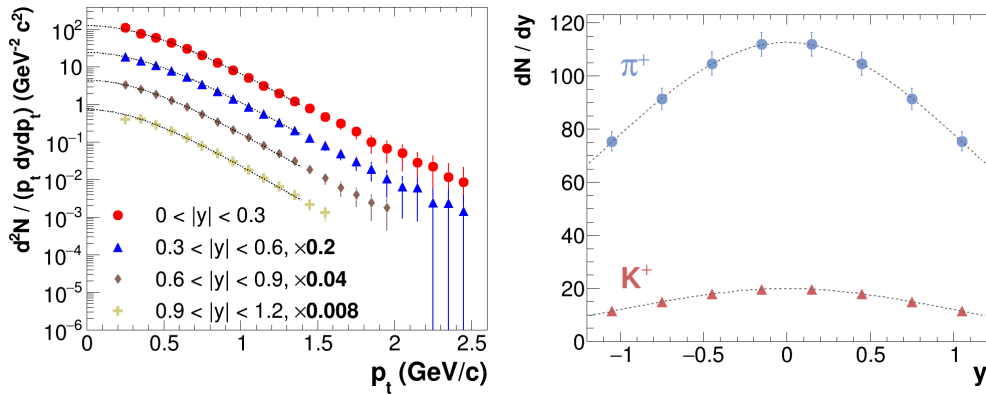


Fig. 4.2.2. (Left panel) Invariant p_T spectra of K^+ from central Au+Au at 8.8 GeV. The midrapidity spectra are drawn to scale; other distributions are scaled down by successive powers of five for clarity. Dashed lines indicate the used fit function. (Right panel) Rapidity distributions of π^+ and K^+ from central Au+Au collisions at 8.8 GeV.

From Gaussian fits (see dashed lines) we found, that from 70% to 90% of the final state phase space for the case of K^+ (from 60% to 80% for the case of π^+) can be covered by the measurements. Moreover, in the extrapolation to the full yield an error in the mean multiplicity of less than 4% for kaons and 3% for pions can be achieved. These errors were estimated as the difference between the value from the full integral of the rapidity spectra and the true multiplicity from the event generator. Thus, the suggested MPD setup has good perspectives for measuring

hadroproduction in A+A collisions potentially unveiling the properties of phase transformation in dense baryon matter at NICA.

4.3. MPD performance for measurement of (multi)strange hyperon production

A PHSD data set of $2 \cdot 10^6$ Au+Au minimum bias events at 11 GeV was partitioned into four centrality bins in terms of the impact parameter interval. Hyperon reconstruction analysis was performed in several transverse momentum intervals of 0.5 GeV/c width. We reconstruct (multi)strange hyperons by combining charged tracks reconstructed in the TPC, first to select a V0-candidate (a characteristic topology of the two opposite charge daughter tracks) and then to match it with one of the secondary pion or kaon candidate. To guarantee that track combinations are associated with real decays we applied several selection criteria. To ensure that the charged tracks are secondary ones, distinct cuts were applied on the minimum value of the impact parameters to the primary vertex. In addition, a pair of tracks was rejected if the distance of closest approach (DCA) in space between the two opposite charged tracks was larger than a given value. Once the secondary vertex position was defined, only those falling within a fiducial region starting from a given distance from the main vertex were kept. Finally, the invariant mass was calculated under the proper hypothesis. The exact values of selection cuts were found by performing a multidimensional scan over the whole set of selection criteria with a requirement to maximize the invariant mass peak significance

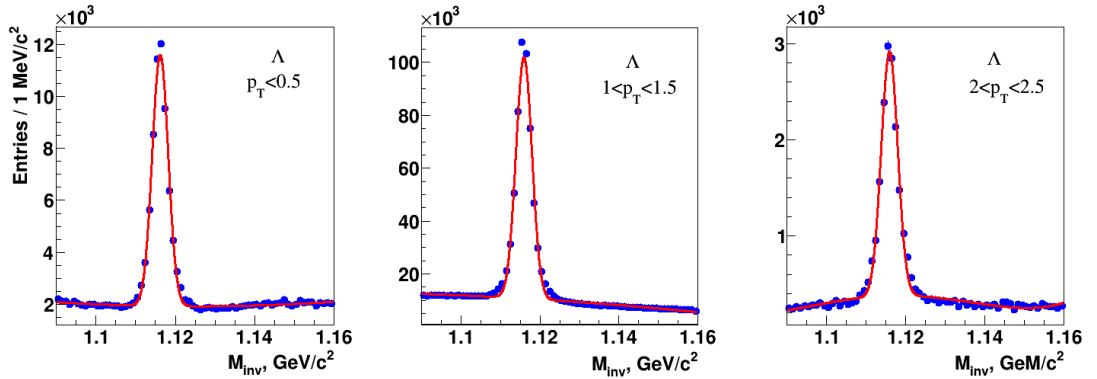


Fig. 4.3.1. Invariant mass spectra of charged pions and protons in several transverse momentum intervals.

In Fig. 4.3.1 invariant mass spectra of charged pion and proton candidates in several transverse momentum bins are shown. The raw yields of (anti)hyperons were then corrected for the detector acceptance and the reconstruction efficiency.

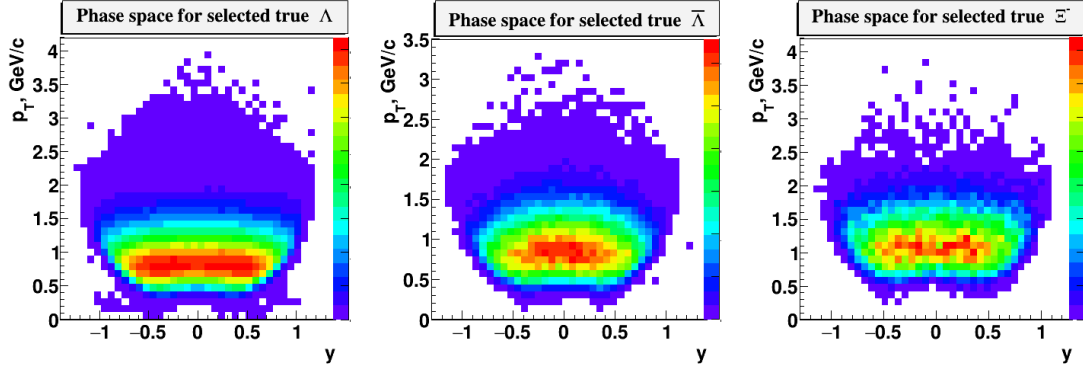


Fig. 4.3.2. MPD detector phase-space for hyperons in central Au+Au collisions at 11 GeV.

In Fig. 4.3.2, the MPD detector phase-space for hyperons is plotted in terms of rapidity and transverse momentum. As one can see, the proposed detector setup has a sufficient coverage to study both the longitudinal and transverse distributions of (anti)hyperons. As an example, in Fig. 4.3.3 the invariant transverse momentum spectra are shown for Lambda in the most central and the most peripheral centrality bin. The distributions were obtained after correcting the raw particle yields in p_T bins by acceptance and efficiency factors determined as described above. The reconstructed yields are plotted with symbols and initial spectra from the model are drawn as histograms. As one can see, the difference between the initial spectra (from the model) and the reconstructed ones is small; the averaged point-by-point difference does not exceed 2%. The reconstructed data are indicated by symbols, while histograms represent the spectra from the model. The solid lines are the thermal fits used for the extrapolation.

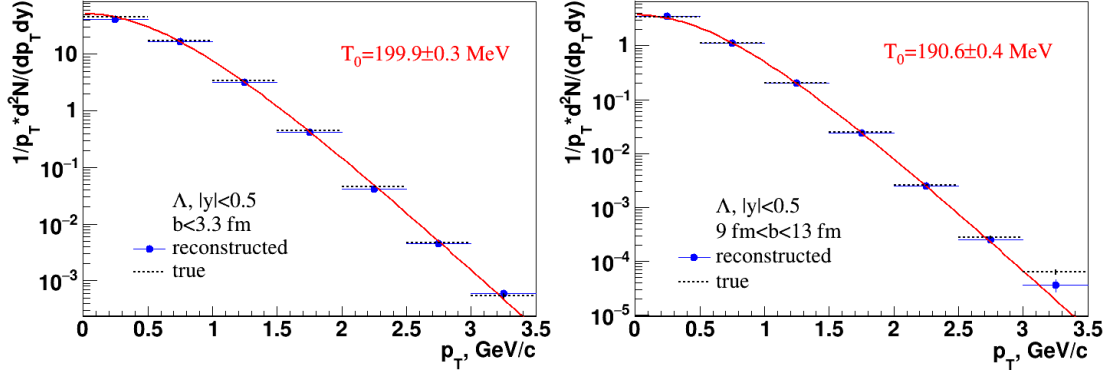


Fig. 4.3.3. The transverse momentum spectra of Lambda within the rapidity range ($|y| < 0.5$) for 0-5% (left panel) and 30-80% (right panel) central Au+Au collisions at 11 GeV.

In order to evaluate expected statistics and phase space coverage at the experiment start-up for rare hyperons (for example anti-Omega) we used the PHSD minimum bias event sample of 8 million Au+Au at 11 GeV. The similar scanning procedure as for Lambda hyperons was used to find the significance maximum. The resulting invariant mass peak can be seen in Fig. 4.3.4 (left panel) along with the rapidity - transverse momentum phase space distributions for correctly reconstructed hyperons after final selection (right panel). One can see that the invariant mass peaks are clearly visible and the detector provides sufficient hyperon coverage at mid-rapidity.

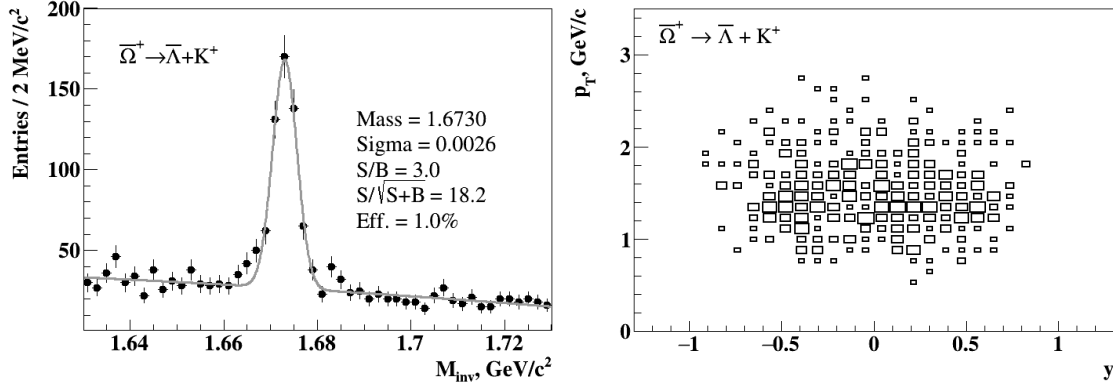


Fig. 4.3.4. Reconstructed invariant mass of anti-Omega (left) and its phase-space (right).

4.4. Direct and elliptic flow measurements at NICA/MPD

The anticipated performance of the MPD detector for the directed flow measurements of charged pions, kaons and protons is demonstrated in the Fig. 4.4.1. A sample of 5M minimum-bias Au+Au collisions at 5 GeV (left panel) and 11 GeV (right panel) simulated with UrQMD event generator was used for the analysis. The MPD detector response was simulated using GEANT4 toolkit and the resulting signals from the detector subsystems were used as input information for the full reconstruction procedure, which includes the realistic particle identification in TOF and TPC detectors ($|\eta| < 1.5$) of MPD. The first order event plane was reconstructed using the energy deposition of particles detected in the forward hadronic calorimeters (FHCaL), located at ($2 < |\eta| < 5$).

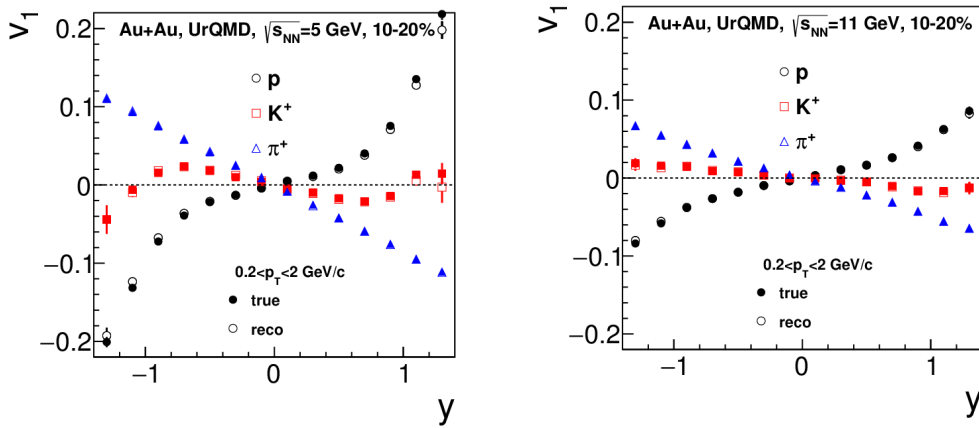


Fig. 4.4.1. Directed flow v_1 for charged pions, kaons and protons as a function of rapidity for Au+Au collisions at 5 GeV (left) and 11 GeV (right). The results from the UrQMD model are marked as true, and the ones from the full reconstruction procedure are marked as reco.

As know from existing experimental data, the excitation function of the directed and elliptic flow from mid-central Au+Au collisions indicate a strong non-monotonic behavior at energies of accelerator facility NICA, thus, the high-statistics differential measurements of v_n as a function of centrality, p_T , rapidity for different particle species anticipated from the MPD expected to provide the valuable information about the properties of strongly interacting matter in this domain of QCD phase diagram.

4.5. Study of electron-positron pairs in A+A collisions at NICA/MPD

A detailed description of the analysis procedure and results can be found in Ref. [5]. Experimental study of dileptons in heavy-ion collisions is a challenging task, because of a huge combinatorial background of uncorrelated lepton pairs from the Dalitz decays of π^0 and γ - γ conversions. The main goal of this study was to investigate MPD detector performance for low-mass dilepton measurements in terms of hadron suppression factor, signal-to-background ratio and invariant mass resolution. We used in this study central (0-3 fm) Au-Au collisions at the center-of-mass energy of 7 GeV from the UrQMD generator in combination with the cocktail of vector mesons from the Pluto event generator. The used detector set-up includes the Time Projection Chamber (TPC), Time-Of-Flight system (TOF) and Electromagnetic Calorimeter (EMC) covering the pseudorapidity range $|\eta| < 1.2$. The particles were transported through the detector by the Geant 3.21 code, the track reconstruction was based on the Kalman filtering technique. All the reconstructed in the TPC tracks were then extrapolated to the TOF detector and matched with TOF hits. The efficiency of track matching with TOF was found to be of about 90% at $p_T > 0.4$ GeV/c, and the transverse momentum resolution appeared to be better than 3% for tracks with p_T below 1 GeV/c. Electron identification was achieved by using combined information about the specific energy loss dE/dx from TPC, time-of-flight from TOF and E/p from EMC. The achieved overall hadron rejection factor was about 3200. The conversion pairs were rejected by a cut, making use of the fact that the magnetic field is orthogonal to the dilepton's momenta plane. This selection was complemented by a cut on the radial position of the production point. In addition, in order to suppress electrons (positrons) from the conversion further we applied a transverse momentum cut: $0.2 < p_T < 2$ GeV/c.

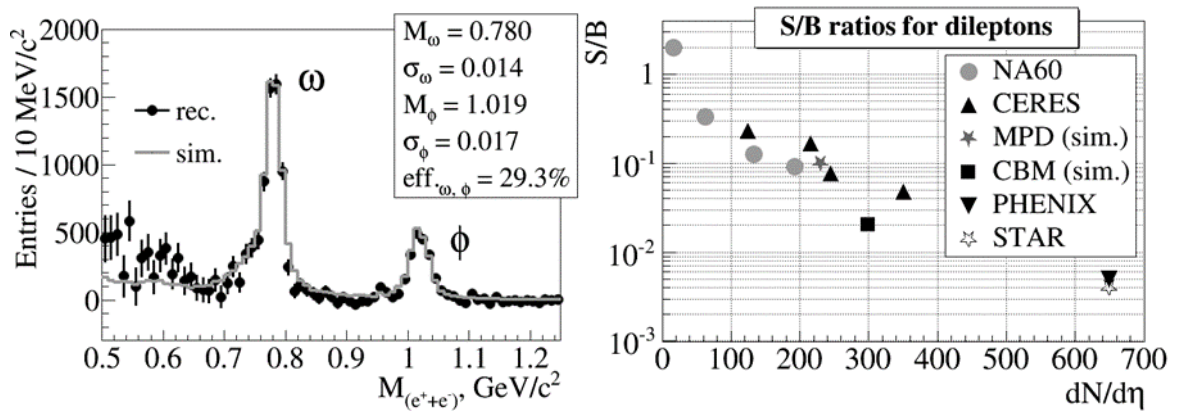


Fig.4.5.1.(Left) Background-subtracted invariant mass distributions of electron-positron pairs from central Au+Au collisions at MPD.(Right) Signal-to-Background (S/B) ratio from heavy-ion experiments as a function of total charged multiplicity.

In Fig. 4.5.1 (left panel) a background-subtracted invariant mass distributions of electron-positron pairs in the pseudorapidity window $|\eta| < 1.0$ is plotted. A rough estimate of invariant mass resolution of the MPD setup was made by fitting the dileptons spectra at the poles for vector mesons: RMS of 14 and 17 MeV were obtained for the omega- and phi-meson pole, respectively. The overall (integrated over the invariant mass window of 0.2-1.5 GeV/c²) signal-to-background ratio was found to be close to 10%. The obtained results for the signal-to-background ratio are shown in Fig. 4.5.1 (right panel) along with the published data from other experiments. The expected parameters of the MPD setup are among the best over the world.

REFERENCES

- [1] <https://git.jinr.ru/nica/mpdroot>
- [2] Fruhwirth, R., Nucl. Instr. and Meth. A 262 (1987) 444.
- [3] Gertsenberger K., Merts S., Rogachevsky O. and Zinchenko A., Eur. Phys. J. A 52 (2016) 214.
- [4] Kolesnikov V., Mudrokh A., Vasendina V. and Zinchenko A., Phys. Part. Nucl. Lett. Vol. 16 (2019) 6.
- [5] V. Vasendina et al. Phys. Part. Nucl. Lett. 2013, V. 10, pp. 769-777.

5.0. Milestones of MPD assembling in 2020-2021

Year 2020	
1. March 1 st -	- MPD Hall and pit are ready to store and unpack Yoke parts
2. April – May	- Magnet Yoke is assembled for alignment checks
3. June	- Solenoid is ready for transportation from ASG (Italy)
4. July - August	- Solenoid is in Dubna
5. August-Sept	- Assembling of Magnet Yoke and Solenoid at JINR
6. July- Sept	- Preparation for switching on the Solenoid
7. Oct-Nov	- Magnetic Field measurement
8. December	- Installation of Support Frame.
Year 2021	
9. Jan - Jul 2021	- Installation of subsystems, Electronics Platform, Cabling
10. Aug 2021	-Commissioning
11. Oct 2021	-Readiness for Cosmic Ray tests

6.0. Funding

Cost Estimate in 2020-2025

	Expenditure items	Full cost	1st year (2021)	2d year (2022)	3d year (2023)	4th year (2024)	5th year (2025)
	Direct expenses for the Project						
1	Nuclotron, Collider, hours	10250	0	250	2500	3500	4000
2	Computing (processor* hour), mln.	165,6	10,8	18,0	28,8	50,4	57,6
3	Computing communication						
4	Technical Design, hours	40000	10000	10000	10000	5000	5000
	Experimental Workshop, hours						
6	Materials k\$	17750	3500	2250	2300	3500	6200
7	Equipment k\$	6108	1203	945	640	1900	1420
8	Payment for research carried out under contracts k\$	2650	750	550	550	400	400
9	Travel allowance, including: k\$	950	200	180	180	190	200
	В т.ч.						
	a) non-rouble zone countries	660	120	120	120	150	150
	б) rouble zone countries	140	30	30	30	25	25
	в) protocol-based	140	30	30	30	25	25
	Total direct expenses	27458	5653	3925	3670	5990	8220